Computers and Fluids 299 (2025) 106730

Contents lists available at ScienceDirect

Computers and Fluids

journal homepage: www.elsevier.com/locate/compfluid

Continued development of an entropy-aware high-order modal Discontinuous Galerkin solver for the Navier–Stokes equations

Luca Alberti [a], Emanuele Carnevali [a],*, Alessandro Colombo [b], Andrea Crivellini [a]

[a] Dipartimento di Ingegneria Industriale e Scienze Matematiche, Università Politecnica delle Marche, via Brecce Bianche 12, Ancona, 60131, Italy
[b] Dipartimento di Ingegneria e Scienze Applicate, Università degli Studi di Bergamo, via A. Einstein, 2, Dalmine (BG), 24044, Italy

ARTICLE INFO

This paper is dedicated to the memory of Prof. Arturo Hidalgo López (*July 03rd 1966 – †August 26th 2024) of the Universidad Politecnica de Madrid, organizer of HONOM 2019 and active participant in many other editions of HONOM. Our thoughts and wishes go to his wife Lourdes and his sister María Jesús, whom he left behind.

Keywords:
Entropy conservation/stability
Modal DG
High-order
DEEB
Bassi–Rebay schemes

ABSTRACT

This paper outlines the development of a fully entropy-aware high-order modal discontinuous Galerkin solver for the Navier–Stokes equations. The entropy conservation/stability of the convective discrete operator is obtained by implementing several variants of the direct enforcement of entropy balance, i.e. DEEB, originally proposed by Abgrall. The tests performed demonstrate that all DEEB variants may be effectively exploited to obtain a considerable boost in robustness over the baseline scheme, enabling the solver to simulate flow configurations that would otherwise be impossible to tackle. On top of this, we derive an entropy stable formulation for the Bassi–Rebay viscous discretizations through a L_2-projection of the viscous fluxes. By coupling the correction introduced for the convective terms with the aforementioned viscous flux projection we are able to construct a fully entropy stable numerical framework. The latter proves to be sufficiently robust to simulate highly challenging flow problems, characterized by abrupt gradients in the thermodynamic variables, in conditions of strong spatial under-resolution.

1. Introduction

High-order Discontinuous Galerkin (DG) schemes offer a highly accurate and efficient numerical framework to simulate fluid dynamics problems. Nonetheless, DG schemes are also known to be prone to robustness issues related to the structural under-integration of non-linear terms. These integration errors are strictly related to the failure of a straightforward enforcing of physical compatibility constraints on the numerically discretized solution. Since the enforcing of a physically-compatible evolution on the discrete governing equations offers clear advantages in terms of robustness [1–3], several strategies have been developed with this objective. Within nodal DG discretizations, an efficient strategy to address aliasing errors involves employing Summation by Parts (SBP) operators that maintain essential commutation properties of integral operations, e.g. integration by parts. This, coupled with a suitable split formulation of the convective fluxes, led to the derivation of entropy conserving/stable (EC/ES) and kinetic energy preserving (KEP) nodal and modal discretizations [3–9]. The approach we proposed in [2], on the other hand, involves a standard modal DG solver built on a conservative formulation, embedding an entropy projection–correction strategy designed to ensure the entropy conservation/stability of the spatial discretization. The same approach can be used to enforce other properties, such as the previously mentioned KEP property. However, although feasible, the development of a scheme that is simultaneously EC/ES and KEP requires special attention and is left for future work. One of the key ingredients of the approach resides in the introduction of a term [10], to be added to the discrete spatial residuals, designed to explicitly correct the integration errors disrupting a physically consistent evolution of the numerical entropy. In previous contributions [2,11] we verified that the resulting DG approximation guarantees, upon selection of suitable convective numerical fluxes [12], an evolution of the thermodynamic entropy in agreement with physical laws. This, in turn, induced a significant improvement in robustness compared to the underlying baseline scheme, which could be useful when undertaking highly challenging flows.

In this paper, we explore various alternative formulations to distribute the entropy correction term beyond the standard implementation of [10], assessing their convergence, conservation and robustness properties. Additionally, since in our modal DG framework the error spoiling the “correct” implicit entropy discretization is ascribable to the rational character of the pressure, we consider a discretization strategy that recovers entropy stability by acting on the pressure-related error. In particular, we show that this modified DG discretization yields a

---

* Corresponding author.
E-mail address: e.carnevali@staff.univpm.it (E. Carnevali).

https://doi.org/10.1016/j.compfluid.2025.106730
Received 28 March 2025; Received in revised form 11 June 2025; Accepted 12 June 2025
Available online 24 June 2025
0045-7930/© 2025 The Authors. Published by Elsevier Ltd. This is an open access article under the CC BY-NC-ND license (http://creativecommons.org/licenses/by-nc-nd/4.0/).

numerical scheme that retains entropy conservation/stability without any residual correction, although forfeiting momentum conservation.

Finally, noting that multiple strategies may be exploited to enforce a physical compatibility to the discretized convective term, we focus on the entropy-aware character of the DG discretization of the viscous term. The numerical framework exploited here is based on the well-known Bassi–Rebay 2 (BR2) scheme [13], a compact stencil modification of the BR1 [14] with interface jump penalization. We show that, in order to obtain a discrete contribution which is formally entropy stable, i.e. acting as an entropy source, it is necessary to introduce an additional projection operation to get a polynomial representation of the viscous fluxes; by doing so, the entropy stability follows from the definition of the lift operators. We also show that the "projected" entropy stable BR1 and BR2 schemes, here referred to as Π_{BR1} and Π_{BR2}, maintain the accuracy of the underlying modal framework and determines an improvement in robustness for some flow cases. The robustness of the algorithms, in particular, is tested without any limiters or other techniques to enforce the positivity of the thermodynamics variables.

The paper is organized as follows. In Section 2 we outline the numerical framework, focusing on the strategies adopted to construct an entropy conserving/stable discretization together with the time integration scheme. In Section 3 we present the results of the numerical experiments, divided between inviscid (Section 3.1) and viscous (Section 3.2) cases. Finally, concluding remarks are collected in Section 4.

2. Numerical framework

Let us consider the compressible Navier–Stokes equations for the d-dimensional geometrical space

$$\begin{aligned}
&\frac{\partial \rho}{\partial t} + \frac{\partial}{\partial x_j}\left(\rho u_j\right) = 0,\\
&\frac{\partial}{\partial t}\left(\rho u_i\right) + \frac{\partial}{\partial x_j}\left(\rho u_i u_j\right) = -\frac{\partial P}{\partial x_i} + \frac{\partial \tau_{ij}}{\partial x_j}\\
&\frac{\partial}{\partial t}\left(\rho E\right) + \frac{\partial}{\partial x_j}\left(\rho u_j E + P u_j\right) = \frac{\partial}{\partial x_j}\left[u_i \tau_{ij} - q_j\right],
\end{aligned} \tag{1}$$

where $i, j = 1, \dots, d$. Note that Eq. (1) is written for the variation in time of the so-called *conservative variables*, *i.e.*, $\mathbf{q} = [\rho, \rho\mathbf{u}, \rho E]^\top \in \mathbb{R}^{(2+d)}$. Specifically, ρ denotes the density, $\mathbf{u} = [u_1, \dots, u_d]^\top$ stands for the velocity vector and E is the total energy. The pressure P is computed assuming the perfect gas hypothesis $P = \rho R T$, where R is the perfect gas constant and T is the temperature. The calorically perfect gas hypothesis is also used, with the specific heat ratio $\gamma = c_p/c_v$ set to 1.4.

The stress tensor and the heat flux vector of Eq. (1) are provided by

$$\tau_{ij} = \mu\left(\frac{\partial u_i}{\partial x_j} + \frac{\partial u_j}{\partial x_i}\right) + \lambda \frac{\partial u_k}{\partial x_k}\delta_{ij}, \qquad q_j = -\hat{k}\frac{\partial T}{\partial x_j}, \tag{2}$$

respectively, where $\lambda = -2/3\,\mu$. In Eq. (2), $\hat{k}$ is the thermal conductivity and μ the dynamic viscosity, related through the Prandtl number $Pr = c_p\mu/\hat{k}$. The following power-law is used to model the relationship between μ and the local temperature T

$$\mu(T) = \mu_r\left(\frac{T}{T_r}\right)^\beta, \tag{3}$$

where T_r and μ_r are the values of temperature and viscosity at the reference conditions, while β, here equal to 3/4 if not otherwise stated, is the index of the power-law.

The system of governing equations can be written in compact form as

$$\frac{\partial \mathbf{q}}{\partial t} + \frac{\partial \mathbf{F}_{c,i}(\mathbf{q})}{\partial x_i} + \frac{\partial \mathbf{F}_{v,i}(\mathbf{q}, \nabla\mathbf{q})}{\partial x_i} = \mathbf{0} \tag{4}$$

where $i = 1, \dots, d$, and from now on, we assume summation over repeated indices. Here, $\mathbf{F}_c \in \mathbb{R}^{(2+d)\times d}$ and $\mathbf{F}_v \in \mathbb{R}^{(2+d)\times d}$ are the convective and viscous flux functions, respectively. The weak-form of Eq. (4) is obtained upon multiplication by a smooth test function $\boldsymbol{\Phi} \in \mathbb{R}^{2+d}$ and integration over the domain $\Omega \subset \mathbb{R}^d$

$$\begin{aligned}
\int_\Omega \boldsymbol{\Phi}^\top \frac{\partial \mathbf{q}}{\partial t}\, d\Omega - \int_\Omega \left(\frac{\partial \boldsymbol{\Phi}}{\partial x_i}\right)^\top \left(\mathbf{F}_{c,i}(\mathbf{q}) + \mathbf{F}_{v,i}(\mathbf{q}, \nabla\mathbf{q})\right) d\Omega&\\
+ \int_{\partial\Omega} \boldsymbol{\Phi}^\top \left(\mathbf{F}_{c,i}(\mathbf{q}) + \mathbf{F}_{v,i}(\mathbf{q}, \nabla\mathbf{q})\right) n_i\, d\sigma = 0&,
\end{aligned} \tag{5}$$

where integration by part is used, and n_i are the components of the unit normal vector pointing outward from $\partial\Omega$. The domain Ω is then discretized by means of the volume mesh $\mathcal{K}_h = \{K\}$ made of cells K, and the set of mesh faces $\mathcal{F}_h = \mathcal{F}_h^0 \bigcup \mathcal{F}_h^b$ partitioned into subsets of internal $\mathcal{F}_h^0$ and boundary $\mathcal{F}_h^b$ faces. The set $\mathcal{F}_K \subseteq \mathcal{F}_h$, instead, collects $\forall K \in \mathcal{K}_h$ the faces belonging to the element boundary. The functions $\mathbf{q}$ and $\boldsymbol{\Phi}$ are replaced by discontinuous finite element approximations $\mathbf{q}_h, \boldsymbol{\Phi}_h \in \left[\mathcal{V}_h\right]^{d+2}$, where

$$\mathcal{V}_h = \left\{\phi_h \in L_2(\Omega) : \phi_h\big|_K \in \mathbb{P}_d^p(K), \forall K \in \mathcal{K}_h\right\}$$

is the set of piecewise-continuous, pth degree, d-dimensional polynomial functions. As a basis for $\mathcal{V}_h$, the orthonormal and hierarchical set of functions $\left\{\phi_{h,l}\right\}_{l=1}^{N_{\text{DoF}}}$ defined $\forall K \in \mathcal{K}_h$ in the mesh space according to [15] are used, where $N_{\text{DoF}} = \prod_{m=1}^{d}(k+m)/m$. Any numerical function belonging to the discontinuous polynomial space can be formulated in terms of the elements of a global vector of degrees of freedom (DoF). As an example, the κth component of the solution vector $\mathbf{q}_h$ can be expressed as a function of the set of DoF $\mathbf{Q}$ as $q_{h,\kappa} = \phi_{h,l} Q_{\kappa,l}\ \forall K \in \mathcal{K}_h$, where $l = 1, \dots, N_{\text{DoF}}$ and $\kappa = 1, \dots, d+2$. The discontinuous nature of the solution across any face of a cell $F \in \partial K^+ \cap \partial K^-$ leads to the definition of the jump and average trace operators

$$[\![\circ]\!] = \circ^+ - \circ^-, \qquad \{\circ\} = \frac{1}{2}\left(\circ^+ + \circ^-\right). \tag{6}$$

To efficiently provide entropy conservation/stability to the spatial discretization the approach of Alberti et al. [2,11] is pursued, where the solution is sought for the set of the conservative variables $\mathbf{q}_h$, while the space DG discrete operators are evaluated from the L_2-projection of the conservative variables onto the entropy ones $\mathbf{v}_h$. The L_2-projection, in particular, is defined as

$$\int_K \boldsymbol{\Phi}_h^\top \mathbf{v}_h\, d\Omega = \int_K \boldsymbol{\Phi}_h^\top \mathbf{v}\left(\mathbf{q}_h\right) d\Omega, \qquad \forall K \in \mathcal{K}_h, \tag{7}$$

where $\mathbf{v}(\mathbf{q}_h)$ identifies the vector of the entropy variables expressed as rational function of the conservative state $\mathbf{q}_h$. The set of entropy variables can be defined, according to Hughes et al. [16], from the entropy pair

$$\mathcal{S} = -\frac{\rho s}{\gamma - 1} = -\frac{\rho \ln(P\rho^{-\gamma})}{\gamma - 1}, \qquad \sigma_i = u_i \mathcal{S}, \tag{8}$$

which results in

$$\mathbf{v} = \frac{\partial \mathcal{S}}{\partial \mathbf{q}} = \left[\mathrm{v}_1, \dots, \mathrm{v}_{2+d}\right]^\top = \left[\frac{\gamma - s}{\gamma - 1} - \frac{\rho}{2P}|\mathbf{u}|^2, \frac{\rho\mathbf{u}}{P}, -\frac{\rho}{P}\right]^\top. \tag{9}$$

Note that the set of entropy variables of Eq. (9) symmetrizes all terms of the Navier–Stokes equations. Particularly, the viscous terms read

$$\mathbf{F}_{v,i}(\mathbf{v}, \nabla\mathbf{v}) = -\mathbf{K}_{i,j}(\mathbf{v})\frac{\partial \mathbf{v}}{\partial x_j}, \tag{10}$$

where the matrices $\mathbf{K}_{i,j}(\mathbf{v}) \in \mathbb{R}^{(2+d)\times(2+d)}$ assemble into a symmetric positive semi-definite block matrix $\mathbf{K}(\mathbf{v})$, see Appendix.

Ultimately, the DG discretization of the governing equations entails finding, for $\kappa = 1, \dots, 2+d$, the elements of $\mathbf{Q}$ such that

$$\begin{aligned}
\sum_{K\in\mathcal{K}_h} \int_K \phi_{h,l} \frac{d q_{h,\kappa}}{dt}\, d\Omega - \sum_{K\in\mathcal{K}_h} \int_K \frac{\partial \phi_{h,l}}{\partial x_i} F_{\kappa,i}\left(\mathbf{v}_h, \nabla_h \mathbf{v}_h + \mathbf{R}\left([\![\mathbf{v}_h]\!]\right)\right) d\Omega&\\
+ \sum_{F\in\mathcal{F}_h} \int_F [\![\phi_{h,l}]\!]\, \hat{F}_\kappa\left(\mathbf{v}_h^\pm, \nabla\mathbf{v}_h^\pm, \mathbf{n}_F\right) d\sigma = 0&.
\end{aligned} \tag{11}$$

Concerning Eq. (11), the vector $\mathbf{n}_F = \{n_{F,i}\}_{i=1}^{d}$ appearing within the surface integral is the uniquely defined unit normal vector at each considered mesh interface. Therein, as commonly done in DG discretizations, the sum of the physical convective and viscous flux functions $\mathbf{F}$ is replaced by the sum of their numerical counterparts, i.e. $\hat{\mathbf{F}} = \hat{\mathbf{F}}_c + \hat{\mathbf{F}}_v$. Particularly, the entropy conserving flux of Ismail and Roe [17] or the entropy stable Godunov flux computed from the exact Riemann solver of [18] are employed for the convective numerical flux $\hat{\mathbf{F}}_c = \hat{\mathbf{F}}_c(\mathbf{v}_h^{\pm}, \mathbf{n}_F)$. On the other hand, the interface viscous flux discretization follows the BR2 approach of Bassi and Rebay [19], based on a centered numerical flux according to

$$\hat{\mathbf{F}}_v\left(\mathbf{v}_h^{\pm}, \nabla\mathbf{v}_h^{\pm}, \mathbf{n}_F\right) = \left\{\mathbf{F}_{v,i}\left(\mathbf{v}_h, \nabla_h\mathbf{v}_h + \eta_F \mathbf{r}_F(\llbracket\mathbf{v}_h\rrbracket)\right)\right\} n_{F,i}, \tag{12}$$

and the definition of the local $\mathbf{r}_F \in \left[\mathcal{V}_h\right]^d$ and global $\mathbf{R} \in \left[\mathcal{V}_h\right]^d$ lifting operators, such that, for any function $w \in L^2(F)$

$$\sum_{K\in\mathcal{K}_h} \int_K \boldsymbol{\tau}_h^{\top} \mathbf{r}_F(w)\, d\Omega = -\int_F w \left\{\boldsymbol{\tau}_h\right\}^{\top} \mathbf{n}_F\, d\sigma \quad \forall \boldsymbol{\tau}_h \in \left[\mathcal{V}_h\right]^d, \tag{13}$$

with

$$\mathbf{R}(w) = \sum_{F\in\mathcal{F}_h} \mathbf{r}_F(w). \tag{14}$$

In Eq. (12), η_F is a penalty factor that has to be set to a value greater than the number of cell faces, as demonstrated by Arnold et al. in [20].

Notably, the orthonormality of the base functions on the physical space reduces the mass matrix resulting from the discretization of the unsteady term to the identity matrix. The same property greatly simplifies Eq. (7) by decreasing the cost of calculating the coefficients of the polynomial approximation $\mathbf{v}_h \in \left[\mathcal{V}_h\right]^{d+2}$, which become

$$\mathrm{V}_{\kappa,l} = \int_K \phi_{h,l}\, \mathrm{v}_\kappa\left(\mathbf{q}_h\right) d\Omega, \qquad \forall K \in \mathcal{K}_h. \tag{15}$$

2.1. The entropy stability in a discrete DG framework

Hughes et al. [16] showed that discretizing the Navier–Stokes equations in a Galerkin finite element framework using the variables of Eq. (9) induces the global entropy stability condition

$$\int_\Omega \frac{\partial \mathcal{S}}{\partial t}\, d\Omega \le 0. \tag{16}$$

In this context, the entropy potentials $\theta = \mathbf{v}^{\top}\mathbf{q} - \mathcal{S} = \rho$ and $\boldsymbol{\psi} = [\psi_1, \dots, \psi_d]^{\top}$ are introduced, where $\psi_i = \mathbf{v}^{\top}\mathbf{F}_{c,i} - \sigma_i = \rho u_i$ and $\mathbf{q}^{\top} = \partial\theta/\partial\mathbf{v}$, see [21,22]. To prove the entropy stability of the present DG discretization at the discrete level we manipulate Eq. (11), replacing the test function $\boldsymbol{\Phi}_h$ with the approximation $\mathbf{v}_h \in \left[\mathcal{V}_h\right]^{2+d}$ and substituting the viscous numerical flux defined in Eq. (12) so as to obtain

$$\begin{aligned}
&\sum_{K\in\mathcal{K}_h} \int_K \mathbf{v}_h^{\top} \frac{\partial \mathbf{q}_h}{\partial t}\, d\Omega - \sum_{K\in\mathcal{K}_h} \int_K \left(\frac{\partial \mathbf{v}_h}{\partial x_i}\right)^{\top} \mathbf{F}_{c,i}\left(\mathbf{v}_h\right) d\Omega \\
&- \sum_{K\in\mathcal{K}_h} \int_K \left(\frac{\partial \mathbf{v}_h}{\partial x_i}\right)^{\top} \mathbf{F}_{v,i}\left(\mathbf{v}_h, \nabla_h\mathbf{v}_h + \mathbf{r}\left(\llbracket\mathbf{v}_h\rrbracket\right)\right) d\Omega \\
&+ \sum_{F\in\mathcal{F}_h} \int_F \llbracket\mathbf{v}_h\rrbracket^{\top} \hat{\mathbf{F}}_c\left(\mathbf{v}_h^{\pm}, \mathbf{n}_F\right) d\sigma \\
&+ \sum_{F\in\mathcal{F}_h} \int_F \llbracket\mathbf{v}_h\rrbracket^{\top} \left\{\mathbf{F}_{v,i}\left(\mathbf{v}_h, \left(\nabla_h\mathbf{v}_h + \eta_F \mathbf{r}_F\left(\llbracket\mathbf{v}_h\rrbracket\right)\right)\right)\right\} n_{F,i}\, d\sigma = 0.
\end{aligned} \tag{17}$$

For the sake of simplicity, in this section we omit the contribution of the boundary conditions to focus exclusively on the core of the spatial discretization. Furthermore, to ease the outline of the demonstrations concerning the entropy stability/conservation of the proposed DG modal discretization, the contribution to the entropy balance coming from the convective and the diffusive discrete operators are treated separately.

2.1.1. The convective discrete contribution to the entropy balance

The derivation of an entropy conserving/stable (EC/ES) discretization for the convective component of Eq. (17) rests on the exactness, at the discrete level, of the following equality

$$\begin{aligned}
\sum_{K\in\mathcal{K}_h} \int_K \frac{\partial \mathbf{v}_h^{\top}}{\partial x_i} \mathbf{F}_{c,i}\left(\mathbf{v}_h\right) d\Omega &= \sum_{K\in\mathcal{K}_h} \int_K \frac{\partial \psi_i\left(\mathbf{v}_h\right)}{\partial x_i} d\Omega \\
&= \sum_{F\in\mathcal{F}_h} \int_F \llbracket\psi_i\left(\mathbf{v}_h\right)\rrbracket n_{F,i}\, d\sigma\,.
\end{aligned} \tag{18}$$

If the commutation of the integrals in Eq. (18) holds true under the chosen quadrature formulae, then it is easy to derive an EC/ES convective discretization upon selection of a suitable interface numerical flux $\hat{\mathbf{F}}_c\left(\mathbf{v}_h^{\pm}, \mathbf{n}_F\right)$ that satisfies Tadmor's condition [12,21,23]

$$\llbracket\mathbf{v}_h\rrbracket^{\top} \hat{\mathbf{F}}_c\left(\mathbf{v}_h^{\pm}, \mathbf{n}_F\right) - \llbracket\psi_i\left(\mathbf{v}_h\right)\rrbracket n_{F,i} \ge 0\,. \tag{19}$$

However, the non-polynomial character of the integrand function appearing in Eq. (18) disrupts the last equality at the discrete level as, in general, the quadrature rule is chosen to integrate exactly only polynomials of order up to $2p$. One possibility to nullify the integration error is the use of Gauss formulae with very high order of exactness, nevertheless this approach is unpractical and not very robust, as shown in [2].

Another way to enforce an entropy conserving/stable discretization for the convective terms is the one outlined in Alberti et al. [2], which is the strategy we employ here. It consists in coupling the L_2–entropy projection with the correction proposed by Abgrall [10]. Particularly, to fix spurious entropy variations, the integration error

$$\begin{aligned}
\alpha_K &= \int_K \frac{\partial \psi_i\left(\mathbf{v}_h\right)}{\partial x_i} d\Omega - \sum_{F\in\mathcal{F}_K} \int_F \psi_i\left(\mathbf{v}_h\right) n_{F,i}\, d\sigma \\
&= \int_K \left(\frac{\partial \mathbf{v}_h}{\partial x_i}\right)^{\top} \mathbf{F}_{c,i}(\mathbf{v}_h) d\Omega - \sum_{F\in\mathcal{F}_K} \int_F \psi_i\left(\mathbf{v}_h\right) n_{F,i}\, d\sigma,
\end{aligned} \tag{20}$$

is added to Eq. (11) through a spreading factor that suitably distributes the correction across the residual DoF as follows

$$\begin{aligned}
&\sum_{K\in\mathcal{K}_h} \int_K \phi_{h,l} \frac{d q_{h,\kappa}}{dt} d\Omega - \sum_{K\in\mathcal{K}_h} \int_K \frac{\partial \phi_{h,l}}{\partial x_i} F_{\kappa,i}\left(\mathbf{v}_h\right) d\Omega \\
&+ \sum_{F\in\mathcal{F}_h} \int_F \llbracket\phi_{h,l}\rrbracket\, \hat{F}_\kappa\left(\mathbf{v}_h^{\pm}, \mathbf{n}_F\right) d\sigma + \underbrace{\sum_{K\in\mathcal{K}_h} \alpha_K \frac{\int_K \phi_{h,l} \overline{\mathrm{v}}_{h,\kappa} d\Omega}{\int_K \overline{\mathrm{v}}_{h,s} \overline{\mathrm{v}}_{h,s} d\Omega}}_{\text{DEEB}} = 0,
\end{aligned} \tag{21}$$

where $\kappa, s = 1, \dots, d{+}2$. Thanks to the use of the set of entropy variables for the evaluation of the space operator $\alpha_K = \mathcal{O}(h_K^{2p+d})$, where h_K is the characteristic element size. In [11] there is a discussion about how a typically larger α_K can be defined for an alternative set of working variables. Note that, being the focus of the section on the discretization of the convective terms, for the sake of compactness only the latter contributions are explicitly considered in Eq. (21). By defining $\overline{\mathbf{v}}_h = \mathbf{v}_h - \mathbf{v}_{h,0}$, where $\mathbf{v}_{h,0}$, is the mean value of $\mathbf{v}_h$, it is then easy to see that the expression

$$\frac{\int_K \phi_{h,l} \overline{\mathrm{v}}_{h,\kappa} d\Omega}{\int_K \overline{\mathrm{v}}_{h,s} \overline{\mathrm{v}}_{h,s} d\Omega} \tag{22}$$

acts on the residuals to evenly distribute the correction among all DoF except the first one, consequently ensuring the conservation of mean flow quantities. The assembly of this "spreading term" simplifies dramatically thanks to the orthonormality of the polynomial basis as it becomes

$$\frac{\int_K \phi_{h,l} \phi_{h,j} V_{\kappa,j}\, d\Omega}{\int_K \phi_{h,j} V_{s,j}\, \phi_{h,\imath} V_{s,\imath}\, d\Omega} = \frac{V_{\kappa,l}}{V_{s,\imath} V_{s,\imath}}, \tag{23}$$

where $\imath, j, l = 2, \dots, N_{\mathrm{DoF}}$.

It is straightforward to note that upon suitable recombination of the test functions $\phi_{h,l}$ in Eq. (21) so as to recover the projected entropy state $\mathbf{v}_h$, it is possible to write

$$\sum_{K\in\mathcal{K}_h}\int_K \mathbf{v}_h \frac{\partial \mathbf{q}_h}{\partial t} d\Omega = \sum_{K\in\mathcal{K}_h}\int_K \left(\frac{\partial \mathbf{v}_h}{\partial x_i}\right)^\top \mathbf{F}_{c,i}\left(\mathbf{v}_h\right) d\Omega - \sum_{F\in\mathcal{F}_h}\int_F [\![\mathbf{v}_h]\!]^\top \hat{\mathbf{F}}_c\left(\mathbf{v}_h^\pm, \mathbf{n}_F\right) d\sigma - \sum_{K\in\mathcal{K}_h} \alpha_K \underbrace{\frac{\int_K \mathbf{v}_h^\top \overline{\mathbf{v}}_h d\Omega}{\int_K \overline{\mathbf{v}}_h^\top \overline{\mathbf{v}}_h d\Omega}}_{=1} \tag{24}$$

and by substituting Eq. (20), one derives

$$\begin{aligned}\sum_{K\in\mathcal{K}_h}\int_K \mathbf{v}_h \frac{\partial \mathbf{q}_h}{\partial t} d\Omega &= \sum_{K\in\mathcal{K}_h}\int_K \left(\frac{\partial \mathbf{v}_h}{\partial x_i}\right)^\top \mathbf{F}_{c,i}\left(\mathbf{v}_h\right) d\Omega \\ &- \sum_{F\in\mathcal{F}_h}\int_F [\![\mathbf{v}_h]\!]^\top \hat{\mathbf{F}}_c\left(\mathbf{v}_h^\pm, \mathbf{n}_F\right) d\sigma \\ &- \sum_{K\in\mathcal{K}_h}\int_K \left(\frac{\partial \mathbf{v}_h}{\partial x_i}\right)^\top \mathbf{F}_{c,i}(\mathbf{v}_h) \\ &+ \sum_{K\in\mathcal{K}_h}\sum_{F\in\mathcal{F}_K}\int_F \psi_i\left(\mathbf{v}_h\right) n_{F,i}\, d\sigma \\ &= -\sum_{F\in\mathcal{F}_h}\int_F \left[[\![\mathbf{v}_h]\!]^\top \hat{\mathbf{F}}_c\left(\mathbf{v}_h^\pm, \mathbf{n}_F\right) - [\![\psi_i\left(\mathbf{v}_h\right)]\!]\, n_{F,i}\right] d\sigma.\end{aligned} \tag{25}$$

Looking at Eq. (25), it is easy to verify that the entropy conservation/stability of the convective discretization is ensured provided that the numerical convective flux $\hat{\mathbf{F}}_c\left(\mathbf{v}_h^\pm, \mathbf{n}_F\right)$ satisfies Tadmor's condition in Eq. (19).

However, note that the approach of Abgrall et al. [24] can account even for the entropy non-aware behavior of a generic numerical flux $\hat{\mathbf{F}}_c(\mathbf{v}_h^\pm, \mathbf{n}_F)$. In fact, defining

$$\begin{aligned}\alpha_K &= \int_K \left(\frac{\partial \mathbf{v}_h}{\partial x_i}\right)^\top \mathbf{F}_{c,i}(\mathbf{v}_h) d\Omega \\ &+ \sum_{F\in\mathcal{F}_K}\int_F \left(\hat{\sigma}_i\left(\mathbf{v}_h^\pm, \mathbf{n}_F\right) - \mathbf{v}_h^\top \hat{\mathbf{F}}_c\left(\mathbf{v}_h^\pm, \mathbf{n}_F\right)\right) d\sigma,\end{aligned} \tag{26}$$

Eq. (21) results in an entropy conserving discretization, regardless of whether Tadmor's condition is satisfied. In this case, however, Eq. (26) clearly requires the additional evaluation of a suitable numerical flux $\hat{\sigma}_i$ for the mathematical entropy $\mathcal{S}$. Despite the moderate computational burden that the explicit evaluation of EC fluxes may introduce due to the logarithmic functions in their definition, see [17,25,26], the formulation of Eq. (26) would result in larger values of α_K. In a previous work [2], we showed that the entropy projection framework, with α_K only accounting for integration errors, significantly enhances robustness compared to a scheme using the set of conservative variables, where α_K also includes interpolation errors between conservative and entropy variables. Therefore, we consider the use of EC fluxes as the optimal solution to enforce the entropy conserving behavior of our scheme. Nonetheless, it is worth noting that Eq. (26) can be useful when EC flux expressions are not available, such as the case of applications involving the equation of state of real gases.

Different approaches to distribute the entropy correction. As shown by Abgrall, the structure of the spreading term in Eq. (22) formally minimizes the magnitude of the correction introduced in each DoF of the residual vector. In Ref. [27], however, the authors suggest an alternative approach for the distribution of this correction. Therein, the term α_K is added to the residual vector through a spreading term that, within an entropy projection framework, assumes the form

$$\frac{\int_K \frac{\partial \phi_{h,l}}{\partial x_i} \mathbf{P}(\mathbf{v}_h) \frac{\partial \mathbf{v}_h}{\partial x_i} d\Omega}{\int_K \frac{\partial \mathbf{v}_h}{\partial x_k}^\top \mathbf{P}(\mathbf{v}_h) \frac{\partial \mathbf{v}_h}{\partial x_k} d\Omega}, \tag{27}$$

where $\mathbf{P}(\mathbf{v}_h)$ identifies the change of variables matrix $\partial\mathbf{q}(\mathbf{v}_h)/\partial\mathbf{v}_h$. Hence, the numerator of Eq. (27) effectively corresponds to the internal volume contribution arising from a weak-form discretization of the Laplacian term $\int_K(\partial\phi_{h,l}/\partial x_i)(\partial\mathbf{q}(\mathbf{v}_h)/\partial x_i)d\Omega$. Since $\mathbf{P}(\mathbf{v}_h)$ is symmetric and positive definite, it ensures Eq. (27) to reduce to unit when substituting the test function vector with the projected entropy state $\mathbf{v}_h$. Moreover, since the gradient operator enters the definition of the spreading term, it is guaranteed by construction that the correction is distributed across all DoF of each equation apart from the first, as $\partial\phi_{h,1}/\partial x_i = 0$. In other words, even this form of the DEEB term does not alter the mean values of the conservative variables $\mathbf{q}_h$. Following the same concept, it is also possible to recast the standard version of the spreading term into a matrix–vector form as

$$\frac{\int_K \phi_{h,l}\, \mathbf{A}(\mathbf{v}_h)\, \overline{\mathbf{v}}_h\, d\Omega}{\int_K \overline{\mathbf{v}}_h^\top\, \mathbf{A}(\mathbf{v}_h)\, \overline{\mathbf{v}}_h\, d\Omega}, \tag{28}$$

In general, for the correction to remain consistent it is sufficient to construct the matrix $\mathbf{A}(\mathbf{v}_h)$ to be positive semi-definite in such a way to guarantee $\int_K \mathbf{x}^\top\mathbf{A}(\mathbf{v}_h)\mathbf{x}d\Omega \geq 0\ \forall\mathbf{x} \in \mathbb{R}^{2+d}$. The latter inequality, notably, holds true even at the discrete level upon adoption of Gauss quadrature formulae with positive weights. In order to understand the effect that different spreading terms have on the solution, we explore several alternatives to the standard implementation:

(a) the variation employed by Gaburro et al. [27], here referred as DEEB$_a$;
(b) the formulation of Eq. (27), named DEEB$_b$, where $\mathbf{P}(\mathbf{v}_h)$ is replaced by the diffusive flux matrix $\mathbf{K}^*_{i,j}(\mathbf{v}_h) = \mu^{-1}\mathbf{K}_{i,j}(\mathbf{v}_h)$ defined below;
(c) the formulation of Eq. (27) that replaces $\mathbf{P}(\mathbf{v}_h)$ with the identity matrix $\mathbb{I}^{(2+d)}$, denoted as DEEB$_c$;
(d) the formulation of Eq. (28) with $\mathbf{A}(\mathbf{v}_h) = \mathbf{P}(\mathbf{v}_h)$, indicated as DEEB$_d$.

Notably, the variants (a), (b) and (d) produce a consistent spreading term from the dimensional point of view (see Table 1). This consideration, however, does not apply to the variant (c) as well as the standard version, hereinafter referred to as DEEB$_{std}$, which may be framed in the form of Eq. (28) with $\mathbf{A}(\mathbf{v}_h) \equiv \mathbb{I}^{(2+d)}$. For these, in particular, it is easy to realize that in the denominator of Eq. (22) the squared entropy variables are summed without caring about dimensional analysis. Furthermore, similarly to what said for DEEB$_a$ at the beginning of the section, also DEEB$_c$ corresponds to the volume component of a DG discretized Laplacian term. In this case, however, the equality $\mathbf{P}_h(\mathbf{v}_h) \equiv \mathbb{I}^{2+d}$ reduces the operator to a form written directly in terms of $\mathbf{v}_h$.

It is worth pointing out that any alternative form of the spreading term other than DEEB$_{std}$ and DEEB$_c$ does not allow for a quadrature free implementation. In those variants, indeed, Eqs. (27) and (28) require the explicit computation of an integral based on Gauss formulae and hence are characterized by a far lower computational efficiency with respect to the standard form.

Another interesting observation comes from the fact that the viscous-like approach that characterizes DEEB$_b$ can be effectively framed as an entropy viscosity approach. Indeed, upon introduction of the entropy correction α_K, each DoF of the residual vector is altered by a quantity that may be written as

$$\mu^* \int_K \frac{\partial \phi_{h,l}}{\partial x_i} \mathbf{K}^*_{i,j}(\mathbf{v}_h) \frac{\partial \mathbf{v}_h}{\partial x_j} d\Omega, \tag{29}$$

Table 1
Summary of the explored DEEB variants together with their main attributes.

Variant	Formulation	Quadrature-free implementation	Dimensional consistency
DEEB$_{std}$	$\bar{\mathbf{v}}_h^\top \, \mathbb{I}^{2+d} \, \bar{\mathbf{v}}_h$	✓	✗
DEEB$_a$	$\frac{\partial \mathbf{v}_h}{\partial x_k}^\top \mathbf{P}(\mathbf{v}_h) \, \frac{\partial \mathbf{v}_h}{\partial x_k}$	✗	✓
DEEB$_b$	$\frac{\partial \mathbf{v}_h}{\partial x_i}^\top \mathbf{K}^*_{i,j}(\mathbf{v}_h) \frac{\partial \mathbf{v}_h}{\partial x_j}$	✗	✓
DEEB$_c$	$\frac{\partial \mathbf{v}_h}{\partial x_k}^\top \, \mathbb{I}^{(2+d)} \, \frac{\partial \mathbf{v}_h}{\partial x_k}$	✓	✗
DEEB$_d$	$\bar{\mathbf{v}}_h^\top \, \mathbf{P}(\mathbf{v}_h) \, \bar{\mathbf{v}}_h$	✗	✓

with $i, j = 1, \dots, d$, $l = 1, \dots, N_{DoF}$ and where

$$\mu^* = \frac{\alpha_K}{\int_K \frac{\partial \mathbf{v}_h^\top}{\partial x_i} \mathbf{K}^*_{i,j}(\mathbf{v}_h) \frac{\partial \mathbf{v}_h}{\partial x_j} d\Omega}\,, \tag{30}$$

behaves as a virtual (entropy) piecewise constant viscosity. Obviously, since the matrices $\mathbf{K}^*_{i,j}(\mathbf{v}_h)$ derive from the scalar multiplication of $\mathbf{K}_{i,j}(\mathbf{v}_h)$, they still form a global block matrix $\mathbf{K}^*(\mathbf{v}_h)$ which is symmetric and positive semi-definite. Essentially, the DEEB$_b$ takes the form of the internal volume part of the DG discretized viscous term evaluated only with the local $V_{\kappa,i}$ variables, thus without any interface jump contribution.

In the following section, details of the viscous discretization will be given. It is easy to note that whilst the denominator of Eq. (30) is always guaranteed to be non-negative, the sign of α_K depends on the committed error and is not known a priori. For this reason, if no control is introduced in the numerical resolution procedure, there could be instances where a negative, anti-diffusive, viscosity could arise. Note that $\alpha_K < 0$ in Eq. (20) corresponds to a numerical discretization that, net of the DEEB correction, leads to a physically coherent decrease of the mathematical entropy. This error can be corrected with the same algorithm developed to prevent the non-physical growth of $\mathcal{S}$. Alternatively, $\alpha_K = \max(0, \alpha_K)$ can be set with the objective of enforcing the entropy balance only in case of an increasing $\mathcal{S}$. This consideration is valid in general, however in the DEEB$_b$ variant it comes out as even more high-sounding since $\alpha_K < 0$ can be thought as introducing a negative "artificial" viscosity. In Section 3 we will show the effect of imposing or not a non-negative α_K.

A few remarks on the entropy "error". It is worth noting an important aspect about the nature of the integration error, α_K in Eq. (20), committed in the implicit recombination of the DG equations when retrieving the entropy relation. As already discussed, the rational character of the volume fluxes does not ensure the commutation between the volume and the surface integral in Eq. (18). In particular, it is possible to show that this feature can be traced back to a specific thermodynamic quantity, namely the pressure. Indeed, if one explicitly writes the expression of the mass flux divergence as a function of the entropy variables set, the following relation may be obtained

$$\frac{\partial \psi_i}{\partial x_i} = \frac{\partial P \mathrm{v}_{h,1+i}}{\partial x_i} = \frac{\partial P}{\partial x_i} \mathrm{v}_{h,1+i} + \frac{\partial \mathrm{v}_{h,1+i}}{\partial x_i} P\,, \tag{31}$$

where both the pressure and its gradient are to be intended as rational functions of the entropy state $\mathbf{v}_h$ and its gradient $\partial \mathbf{v}_h / \partial x_i$. Substituting Eq. (31) into Eq. (20), one gets

$$\alpha_K = \int_K \left(\frac{\partial P}{\partial x_i} \mathrm{v}_{h,1+i} + \frac{\partial \mathrm{v}_{h,1+i}}{\partial x_i} P \right) d\Omega - \sum_{F \in \mathcal{F}_K} \int_F P \mathrm{v}_{h,1+i} n_i d\sigma\,, \tag{32}$$

where it is clear that the integration error comes exclusively from the rational form of the pressure function.

A possibility to circumvent this issue consists in treating in strong form the pressure inside the momentum equations, which means using in Eq. (11) the following approximated relation

$$\sum_{K \in \mathcal{K}_h} \int_K \frac{\partial \phi_{h,l}}{\partial x_i} P \, d\Omega \simeq - \sum_{K \in \mathcal{K}_h} \int_K \phi_{h,l} \frac{\partial P}{\partial x_i} d\Omega + \sum_{F \in \mathcal{F}_h} \int_F \phi_{h,l} \, P \, n_i d\sigma\,. \tag{33}$$

As a matter of fact, this results in an implicitly recombined entropy equation that reads as

$$\begin{aligned} \sum_{K \in \mathcal{K}_h} \int_K \mathbf{v}_h \frac{\partial \mathbf{q}_h}{\partial t} d\Omega + \sum_{K \in \mathcal{K}_h} \int_K \left(\frac{\partial \mathbf{v}_h}{\partial x_i} \right)^\top \tilde{\mathbf{F}}_i(\mathbf{v}_h) d\Omega \\ - \sum_{K \in \mathcal{K}_h} \int_K \mathrm{v}_{h,1+i} \frac{\partial P}{\partial x_i} d\Omega \\ + \sum_{F \in \mathcal{F}_h} \int_F \mathrm{v}_{h,1+i} \, P \, n_i d\sigma \\ + \sum_{F \in \mathcal{F}_h} \int_F [\![\mathbf{v}_h]\!]^\top \hat{\mathbf{F}}_c(\mathbf{v}_h^\pm, \mathbf{n}_F) d\sigma = 0\,, \end{aligned} \tag{34}$$

with $\tilde{\mathbf{F}}_i(\mathbf{v}_h)$ being the ith Cartesian component of the volume fluxes, freed from the pressure contribution in the momentum equations. The second integrand of Eq. (34) contracts to $\mathrm{v}_{h,1+i} \partial P / \partial x_i$ and cancels out with the third term, whose presence directly arises from the strong-form discretization of the pressure. From this observation, it is easy to verify that the resulting spatial discretization ensures entropy conservation/stability at the discrete level for a suitable choice of the numerical flux. It is worth to remark, however, that this comes at the cost of forfeiting the conservative property of the scheme in the momentum equations. Indeed, the governing equations for the mean momentum component, namely the ones associated to the first DoF for our orthonormal and hierarchical basis, include a generally nonzero contribution owed to the integral of the pressure terms, i.e.

$$\phi_{h,1} \left(- \int_K \frac{\partial P}{\partial x_i} d\Omega + \sum_{F \in \mathcal{F}_K} \int_F P \, n_i d\sigma \right)\,, \tag{35}$$

that spoils the conservative formulation of the standard weak form. In this sense, the integration error is essentially shifted into the momentum equations.

2.1.2. The viscous discrete contribution to the entropy balance

As far as the viscous discretization is concerned, some notable examples of entropy analysis for the BR2 scheme may be found in [28–30], however they do not consider the case in which $\mathbf{K}_{i,j}(\mathbf{v}_h)$ is rational.

In order to extend their analysis, the symmetrized expression of the viscous fluxes of Eq. (12) is substituted into Eq. (17). In doing so, the "induced" entropy equation becomes

$$\begin{aligned} \sum_{K \in \mathcal{K}_h} \int_K \mathbf{v}_h^\top \frac{\partial \mathbf{q}_h}{\partial t} d\Omega + \sum_{K \in \mathcal{K}_h} \int_K \left(\frac{\partial \mathbf{v}_h}{\partial x_i} \right)^\top \mathbf{K}_{i,j}(\mathbf{v}_h) \left(\frac{\partial \mathbf{v}_h}{\partial x_j} \right) d\Omega \\ + \sum_{K \in \mathcal{K}_h} \int_K \left(\frac{\partial \mathbf{v}_h}{\partial x_i} \right)^\top \mathbf{K}_{i,j}(\mathbf{v}_h) \, \mathbf{R}_j([\![\mathbf{v}_h]\!]) \, d\Omega \\ - \sum_{F \in \mathcal{F}_h} \int_F [\![\mathbf{v}_h]\!]^\top \left\{ \mathbf{K}_{i,j}(\mathbf{v}_h) \left(\frac{\partial \mathbf{v}_h}{\partial x_j} + \eta_F \mathbf{r}_{F,j}([\![\mathbf{v}_h]\!]) \right) n_j \right\} d\sigma = 0\,, \end{aligned} \tag{36}$$

where the contribution of the convective terms cancels out upon introduction of the DEEB correction.

The rational character of $\mathbf{K}_{i,j}(\mathbf{v}_h)$ does not allow the last integral of Eq. (36) to be exactly transformed into a volume contribution through the lift operator of Eq. (13), as the identity requires the integrand functions to be defined in a polynomial space. To obviate this, we introduce the L_2-projection

$$\int_K \mathbf{\Phi}_h^\top \mathbf{\Pi}_{F,i} d\Omega = \int_K \mathbf{\Phi}_h^\top \mathbf{K}_{i,j}(\mathbf{v}_h) \left(\frac{\partial \mathbf{v}_h}{\partial x_j} + \eta_F \mathbf{r}_{F,j}([\![\mathbf{v}_h]\!]) \right) d\Omega\,, \tag{37}$$

so that we can define the polynomial viscous flux tensor $\mathbf{\Pi}_F \in \left[\mathcal{V}_h\right]^{d \times (2+d)}$ at each face $F \in \mathcal{F}_K$ of every mesh element $K \in \mathcal{K}_h$. By using the projected viscous flux in the calculation of the surface integral of Eq. (36) and leveraging the local lift definition of Eq. (13), we obtain

$$
\begin{aligned}
&\sum_{K\in\mathcal{K}_h}\int_K \mathbf{v}_h^\top \frac{\partial \mathbf{q}_h}{\partial t}\,d\Omega + \sum_{K\in\mathcal{K}_h}\int_K \left(\frac{\partial \mathbf{v}_h}{\partial x_i}\right)^\top \mathbf{K}_{i,j}(\mathbf{v}_h)\left(\frac{\partial \mathbf{v}_h}{\partial x_j}\right) d\Omega \\
&\qquad + \sum_{K\in\mathcal{K}_h}\int_K \left(\frac{\partial \mathbf{v}_h}{\partial x_i}\right)^\top \mathbf{K}_{i,j}(\mathbf{v}_h)\,\mathbf{R}_j(\llbracket \mathbf{v}_h\rrbracket)\,d\Omega \\
&\qquad + \sum_{K\in\mathcal{K}_h}\sum_{F\in\mathcal{F}_K}\int_K \mathbf{r}_{F,i}^\top(\llbracket \mathbf{v}_h\rrbracket)\,\mathbf{\Pi}_{F,i}\,d\Omega = 0\,.
\end{aligned}
\tag{38}
$$

At this point, the polynomial character of $\mathbf{r}_F(\llbracket \mathbf{v}_h\rrbracket)$ may be exploited in conjunction with the definition of the projection operation of Eq. (37) to write

$$
\begin{aligned}
&\sum_{K\in\mathcal{K}_h}\int_K \mathbf{v}_h^\top \frac{\partial \mathbf{q}_h}{\partial t}\,d\Omega + \sum_{K\in\mathcal{K}_h}\int_K \left(\frac{\partial \mathbf{v}_h}{\partial x_i}\right)^\top \mathbf{K}_{i,j}(\mathbf{v}_h)\left(\frac{\partial \mathbf{v}_h}{\partial x_j}\right) d\Omega \\
&+ \sum_{K\in\mathcal{K}_h}\int_K \left(\frac{\partial \mathbf{v}_h}{\partial x_i}\right)^\top \mathbf{K}_{i,j}(\mathbf{v}_h)\,\mathbf{R}_j(\llbracket \mathbf{v}_h\rrbracket)\,d\Omega \\
&+ \sum_{K\in\mathcal{K}_h}\sum_{F\in\mathcal{F}_K}\int_K \mathbf{r}_{F,i}^\top(\llbracket \mathbf{v}_h\rrbracket)\,\mathbf{K}_{i,j}(\mathbf{v}_h)\left(\frac{\partial \mathbf{v}_h}{\partial x_j} + \eta_F\,\mathbf{r}_{F,j}(\llbracket \mathbf{v}_h\rrbracket)\right) d\Omega = 0\,.
\end{aligned}
\tag{39}
$$

Finally, by introducing the global lift definition of Eq. (14), Eq. (39) can be recast as

$$
\begin{aligned}
\sum_{K\in\mathcal{K}_h}\int_K \mathbf{v}_h^\top \frac{\partial \mathbf{q}_h}{\partial t}\,d\Omega = &- \sum_{K\in\mathcal{K}_h}\int_K \left(\frac{\partial \mathbf{v}_h}{\partial x_i}\right)^\top \mathbf{K}_{i,j}(\mathbf{v}_h)\left(\frac{\partial \mathbf{v}_h}{\partial x_j}\right) d\Omega \\
&- \sum_{K\in\mathcal{K}_h}\int_K \left(\frac{\partial \mathbf{v}_h}{\partial x_i}\right)^\top \mathbf{K}_{i,j}(\mathbf{v}_h)\,\mathbf{R}_j(\llbracket \mathbf{v}_h\rrbracket)\,d\Omega \\
&- \sum_{K\in\mathcal{K}_h}\int_K \mathbf{R}_i(\llbracket \mathbf{v}_h\rrbracket)\,\mathbf{K}_{i,j}(\mathbf{v}_h)\left(\frac{\partial \mathbf{v}_h}{\partial x_j}\right) d\Omega \\
&- \sum_{K\in\mathcal{K}_h}\eta_F\sum_{F\in\mathcal{F}_K}\int_K \mathbf{r}_{F,i}^\top(\llbracket \mathbf{v}_h\rrbracket)\mathbf{K}_{i,j}(\mathbf{v}_h)\mathbf{r}_{F,j}(\llbracket \mathbf{v}_h\rrbracket)d\Omega\,,
\end{aligned}
\tag{40}
$$

with $i,j = 1,\ldots,d$.

Note that the introduction of an approximate polynomial representation of the viscous fluxes ensures the exactness of Eq. (40) at the discrete level, provided that suitably accurate quadrature formulae are used. However, Eq. (40) in the current form does not pose any strict bound on the time evolution of the discrete mathematical entropy for the system under exam. For that to be the case, it is necessary to lean on the theoretical results outlined in [28,30]. Specifically, the Lemma generalizing Young's inequality, defined in [30] as *Lemma 4.7*, is needed. The Lemma reads as

Lemma 1. *If* $\mathbf{A}\in\mathbb{R}^{n\times n}$ *is a symmetric positive semi-definite matrix, then there holds for arbitrary vectors* $\mathbf{a},\mathbf{b}\in\mathbb{R}^n$ *and* $\epsilon > 0$

$$
2\left(\mathbf{a}^\top\mathbf{A}\mathbf{b}\right) \le \epsilon\left(\mathbf{a}^\top\mathbf{A}\mathbf{a}\right) + \frac{1}{\epsilon}\left(\mathbf{b}^\top\mathbf{A}\mathbf{b}\right)\,.
\tag{41}
$$

Since the matrix $\mathbf{K}_{i,j}(\mathbf{v}_h)$ is symmetric and positive semi-definite, Lemma 1 can be applied to show that Eq. (40) is bounded from above as

$$
\begin{aligned}
&\sum_{K\in\mathcal{K}_h}\int_K \frac{\partial S(\mathbf{q}_h)}{\partial t}\,d\Omega \le -(1+\epsilon)\sum_{K\in\mathcal{K}_h}\int_K \left(\frac{\partial \mathbf{v}_h}{\partial x_i}\right)^\top \mathbf{K}_{i,j}(\mathbf{v}_h)\left(\frac{\partial \mathbf{v}_h}{\partial x_j}\right) d\Omega \\
&- \frac{1}{\epsilon}\sum_{K\in\mathcal{K}_h}\int_K \mathbf{R}_i^\top(\llbracket \mathbf{v}_h\rrbracket)\mathbf{K}_{i,j}(\mathbf{v}_h)\mathbf{R}_j(\llbracket \mathbf{v}_h\rrbracket)d\Omega \\
&\;- \sum_{K\in\mathcal{K}_h}\eta_F\sum_{F\in\mathcal{F}_K}\int_K \mathbf{r}_{F,i}^\top(\llbracket \mathbf{v}_h\rrbracket)\mathbf{K}_{i,j}(\mathbf{v}_h)\,\mathbf{r}_{F,j}(\llbracket \mathbf{v}_h\rrbracket)d\Omega\,, \quad \forall\epsilon > 0.
\end{aligned}
\tag{42}
$$

The structure of $\mathbf{K}_{i,j}(\mathbf{v}_h)$ guarantees that, short of the negative sign, the terms on the right-hand side of the inequality contribute positively at each local Gauss point. This property ensures that the BR2 discretization supports an entropy stable, i.e. non-increasing, evolution of the discrete mathematical entropy as its time derivative is bounded from above by a sum of negative terms. It is important to emphasize, however, that this result holds true only when the viscous fluxes are projected onto the DG polynomial space of the solution. Without this projection the integral transformations involving the total and local lift operators would not be strictly valid because, as already said for the last integral of Eq. (36), they require the operations to be defined between polynomial spaces.

The proof procedure presented above may be readily adjusted to further show the entropy stability of the BR1 discretization scheme. Although several demonstrations may be found within nodal DG frameworks, e.g. [31], what we propose here is the proof of the entropy stability of the BR1 in our modal DG scheme. First, we write the surface viscous contribution in Eq. (36) using the global lift operator, obtaining

$$
\begin{aligned}
&\sum_{K\in\mathcal{K}_h}\int_K \mathbf{v}_h^\top \frac{\partial \mathbf{q}_h}{\partial t}\,d\Omega + \sum_{K\in\mathcal{K}_h}\int_K \left(\frac{\partial \mathbf{v}_h}{\partial x_i}\right)^\top \mathbf{K}_{i,j}(\mathbf{v}_h)\left(\frac{\partial \mathbf{v}_h}{\partial x_j} + \mathbf{R}_j(\llbracket \mathbf{v}_h\rrbracket)\right) d\Omega \\
&- \sum_{F\in\mathcal{F}_h}\int_F \llbracket \mathbf{v}_h\rrbracket^\top \left\{ \mathbf{K}_{i,j}(\mathbf{v}_h)\left(\frac{\partial \mathbf{v}_h}{\partial x_j} + \mathbf{R}_j(\llbracket \mathbf{v}_h\rrbracket)\right) n_j \right\}\, d\sigma = 0\,.
\end{aligned}
\tag{43}
$$

Then, by defining the viscous flux projection as

$$
\int_K \mathbf{\Phi}_h^\top \mathbf{\Pi}_i\,d\Omega = \int_K \mathbf{\Phi}_h^\top \mathbf{K}_{i,j}(\mathbf{v}_h)\left(\frac{\partial \mathbf{v}_h}{\partial x_j} + \mathbf{R}_j(\llbracket \mathbf{v}_h\rrbracket)\right) d\Omega\,,
\tag{44}
$$

and using it in the computation of the interface viscous fluxes, the viscous terms of Eq. (43) become

$$
\begin{aligned}
&\sum_{K\in\mathcal{K}_h}\int_K \left(\frac{\partial \mathbf{v}_h}{\partial x_i}\right)^\top \mathbf{K}_{i,j}(\mathbf{v}_h)\left(\frac{\partial \mathbf{v}_h}{\partial x_j} + \mathbf{R}_j(\llbracket \mathbf{v}_h\rrbracket)\right) d\Omega \\
&- \sum_{F\in\mathcal{F}_h}\int_F \llbracket \mathbf{v}_h\rrbracket^\top \left\{\mathbf{\Pi}_j n_j\right\} d\sigma\,,
\end{aligned}
\tag{45}
$$

which can then be rewritten rigorously as

$$
\begin{aligned}
&\sum_{K\in\mathcal{K}_h}\int_K \left(\frac{\partial \mathbf{v}_h}{\partial x_i}\right)^\top \mathbf{K}_{i,j}(\mathbf{v}_h)\left(\frac{\partial \mathbf{v}_h}{\partial x_j} + \mathbf{R}_j(\llbracket \mathbf{v}_h\rrbracket)\right) d\Omega \\
&+ \sum_{K\in\mathcal{K}_h}\int_K \mathbf{R}_i^\top(\llbracket \mathbf{v}_h\rrbracket)\,\mathbf{\Pi}_i\,d\Omega\,.
\end{aligned}
\tag{46}
$$

Since the flux projection is defined by construction in the same DG polynomial space of the global lift operator, Eq. (46) causes Eq. (43) to reduce to

$$
\begin{aligned}
&\sum_{K\in\mathcal{K}_h}\int_K \frac{\partial S(\mathbf{q}_h)}{\partial t}\,d\Omega = \\
&- \sum_{K\in\mathcal{K}_h}\int_K \left(\frac{\partial \mathbf{v}_h}{\partial x_i} + \mathbf{R}_i(\llbracket \mathbf{v}_h\rrbracket)\right)^\top \mathbf{K}_{i,j}(\mathbf{v}_h)\left(\frac{\partial \mathbf{v}_h}{\partial x_j} + \mathbf{R}_j(\llbracket \mathbf{v}_h\rrbracket)\right) d\Omega \le 0,
\end{aligned}
\tag{47}
$$

where it is immediate to derive, thanks to the positive semi-definiteness of the symmetric matrix $\mathbf{K}_{i,j}(\mathbf{v}_h)$, that the BR1 discretization actually imposes a bounded evolution of the discrete mathematical entropy.

It is worth to underline that there is a clear difference between the entropy stability of the BR1 and BR2 discretizations. The demonstration for the BR1 yields an exact expression for the time evolution of the global discrete mathematical entropy, as it can be appreciated from Eq. (47). The analysis done for the BR2, instead, establishes just a negative upper bound for the entropy evolution without identifying a precise contribution to entropy production by the viscous discrete operators, see Eq. (42).

Moreover, we note that the standard η_F stability requirement for the BR2 scheme, i.e., $\eta_F \ge \mathrm{card}(\mathcal{F}_K) + 1$, is not altered by the proposed implementation. In fact, it is easy to see that the discretization of the Laplace operator does not change after the projection procedure; therefore, the classical results obtained for the case by Brezzi et al. [13]

still hold true. Nonetheless, from the authors' experience, as well as that of other research groups [3,32], smaller values can be adopted in many cases without compromising the stability of the scheme. For more details, see Section 3.2.2.

2.2. Time integration

By computing the integrals in Eq. (21) and assembling all the elemental contributions we obtain the system of Ordinary Differential Equations (ODEs) that governs the temporal evolution of the discrete solution

$$\frac{d\mathbf{Q}}{dt} + \mathbf{R}\left(\mathbf{Q}\right) = \mathbf{0}. \tag{48}$$

The nonlinear system is integrated in time through an explicit Strong Stability Preserving Runge–Kutta (SSPRK) method [33] characterized by

$$\begin{aligned} \mathbf{Y}_i &= \mathbf{Q}^n + \Delta t \sum_{j=1}^{i-1} a_{ij} \mathbf{R}\left(\mathbf{Y}_j\right), \\ \mathbf{Q}^{n+1} &= \mathbf{Q}^n + \Delta t \sum_{j=1}^{s} b_j \mathbf{R}\left(\mathbf{Y}_j\right), \end{aligned} \tag{49}$$

where s is the number of stages and a_{ij}, b_j are the real coefficients of the scheme reported in [33]. For all simulations presented in this paper the fourth-order five-stage SSPRK scheme is used. The solver allows for the selection of either the time step size or the CFL number. In the latter case, $\Delta t = \min_{K\in\mathcal{K}_h}(\Delta t_K)$, where $\Delta t_K = \mathrm{CFL}\left[h_K/(\mathtt{c}_K + \mathtt{d}_K)\right]$. The characteristic element size is defined as $h_K = d|K|/|\partial K|$, with $|K|$ being the cell area/volume and $|\partial K|$ the measure of its boundary. The convective eigenvalue for each element is computed as $\mathtt{c}_K = \sqrt{\gamma p_{K,0}/\rho_{K,0}} + |\mathbf{u}_{K,0}|$, where the subscript "0" denotes the cell mean values, while the diffusive contribution is determined by $\mathtt{d}_K = 2\left[\mu(T_{K,0}) + \zeta(T_{K,0})\right]/(\rho_{K,0}\, h_K)$, where $\zeta(T) = \hat{k}(T)/c_p$ is the thermal diffusivity.

3. Numerical experiments

3.1. Results of the inviscid test cases

In a previous work [2] we showed that the projection–correction approach allows to retain the conservation of the standard quantities (mass, momentum and total energy), while also discretely ensuring a physically compatible evolution of the entropy. Moreover, we demonstrated that while the order of (spatial/temporal) accuracy of the resulting scheme is not altered, there is a sensible boost in robustness over the baseline conservative framework where all discrete operators are assembled with $\mathbf{q}_h$. Herein, we consider as the baseline version the discretization based on the sole projection operation, i.e. the one where the residual vector is constructed using $\mathbf{v}_h$, without any form of entropy correction. For the sake of compactness, hereinafter we refer to this version as STD.

In this section, we focus on showing the convergence, conservation and robustness of the alternative strategies outlined in , responsible for the entropy conservation/stability of the discretized convective terms. Particularly, the conservation and convergence results are obtained with a fixed CFL sufficiently low so as to isolate the space discretization effects and make time-related errors negligible. All simulations to test robustness, instead, are carried out with $\mathrm{CFL} = 2.5 \cdot 10^{-2}$.

3.1.1. Convergence and conservation properties

In order to verify the theoretical convergence rate of the different solution strategies and their ability to conserve field variables, the following error metrics are defined

$$\eta(\circ, \bullet_{ref}) = (\Omega_h)^{-1/2} ||\circ - \bullet_{ref}||_{L_2}, \tag{50}$$

$$\varepsilon(\circ, \bullet_{ref}) = \Omega_h^{-1} \left| \int_{\Omega_h} \circ \, d\Omega - \int_{\Omega_h} \bullet_{ref} \, d\Omega \right|, \tag{51}$$

where $\circ$ and $\bullet_{ref}$ are the numerical solution and the reference state, respectively. The latter is computed as the L_2–projection of the initial condition onto the DG space.

For this analysis, the 2D Isentropic Vortex Convection (IVC) flow problem is chosen, Refs. [34–36]. The flow consists of a vortical perturbation generated at the center of a doubly periodic square domain that is convected along its diagonal. The periodicity on both sides ensures the conservation/dissipation of ρs as long as the scheme is entropy conserving/stable. The initialized fields are defined by

$$\begin{aligned} u_1 &= \sqrt{\gamma} - \frac{\alpha}{2\pi}\left(x_2 - x_{2_0}\right) e^{\beta(1-r^2)}, \\ u_2 &= \sqrt{\gamma} + \frac{\alpha}{2\pi}\left(x_1 - x_{1_0}\right) e^{\beta(1-r^2)}, \\ P &= \rho^{\gamma}, \\ \rho &= \left(1 - \frac{\alpha^2(\gamma-1)}{16\beta\gamma\pi^2} e^{2\beta(1-r^2)}\right)^{\frac{1}{\gamma-1}}, \end{aligned} \tag{52}$$

where $(x_{1_0}, x_{2_0}) = (5, 5)$, $r = \|x_i - x_{i_0}\|_{L_2}$ and with $\alpha = 5$ and $\beta = 1/2$ dictating the strength of the vortex. This configuration corresponds to a free stream characterized by a Mach number $M = \sqrt{2}$. The $[0, 10]^2$ computational domain is discretized using Cartesian grids made of 25×25 (*coarse*), 50×50 (*medium*) and 100×100 (*fine*) elements. Simulations are advanced in time up to $t_f = 10/\sqrt{\gamma}$, corresponding to one period of vortex revolution, using DG polynomial approximations of order $p = \{3, 4\}$. An entropy conserving (EC) and an entropy stable (ES) variant are considered for the numerical flux function; a discussion on the subject may be found in [37]. The former variant is the one proposed by Ismail and Roe [17], whereas the latter uses a Godunov flux with the exact Riemann solver of Gottlieb and Groth [38]. The spatial convergence is investigated by monitoring the error on the first variable of the solution vector $\mathbf{q}_h$ for the aforementioned spatial discretizations. Having verified that the various DEEB implementations are characterized by similar results, here we report only the viscous-like implementation DEEB$_b$ alongside the standard version DEEB$_{std}$, which is taken as the baseline.

Fig. 1 collects the convergence results for DEEB$_{std}$ (Fig. 1(a)), DEEB$_b$ (Fig. 1(b)) and the strong-form pressure strategy (Fig. 1(c)). While the first and the last strategy exhibit very akin results, DEEB$_b$ produces a slight improvement of the EC flux convergence with respect to both DEEB$_{std}$ and the pressure-based approach. Nonetheless, analogously to what was reported in [2], all plots in Fig. 1 illustrate that the different strategies preserve the rate of convergence of the scheme, which is $p + 1$ for the Godunov entropy stable flux and p for the Ismail&Roe entropy conserving flux.

As far as the conservation properties are concerned, Fig. 2 shows the behavior of the entropy conservation error relatively to the spatial refinements for both DEEB$_b$ and the pressure-based modification. We note that the use of the ES flux of [18] leads to conservation errors with a superconvergent character, having a convergence rate of $2p + 1$ for both strategies in exam. On the other hand, the use of the EC flux of [17] results in an exact conservation of the entropy for both spatial discretizations. While this result is somewhat to be expected for the DEEB$_b$ strategy considering what was found for DEEB$_{std}$ in [2], the curves derived for the pressure-based approach provide the numerical proof that the pressure is indeed the driving contribution of the integration error; as such, its elimination results in a discrete framework

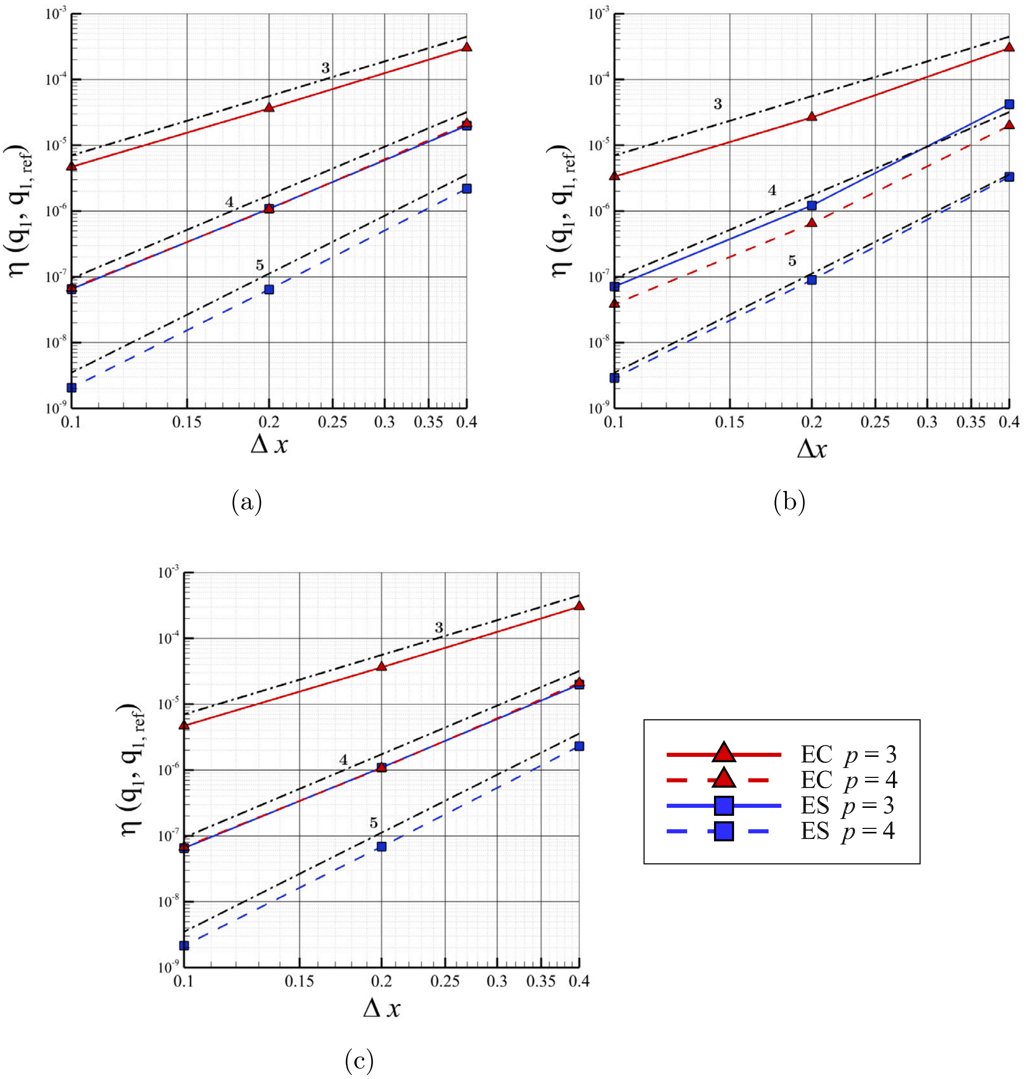

(a)

(b)

(c)

Fig. 1. IVC — spatial refinement test. Errors η on the first variable of vector $\mathbf{q}$. Simulations integrated in time via the explicit SSPRK35. (a) DEEB$_{std}$, (b) DEEB$_b$ and (c) strong-form pressure modification.

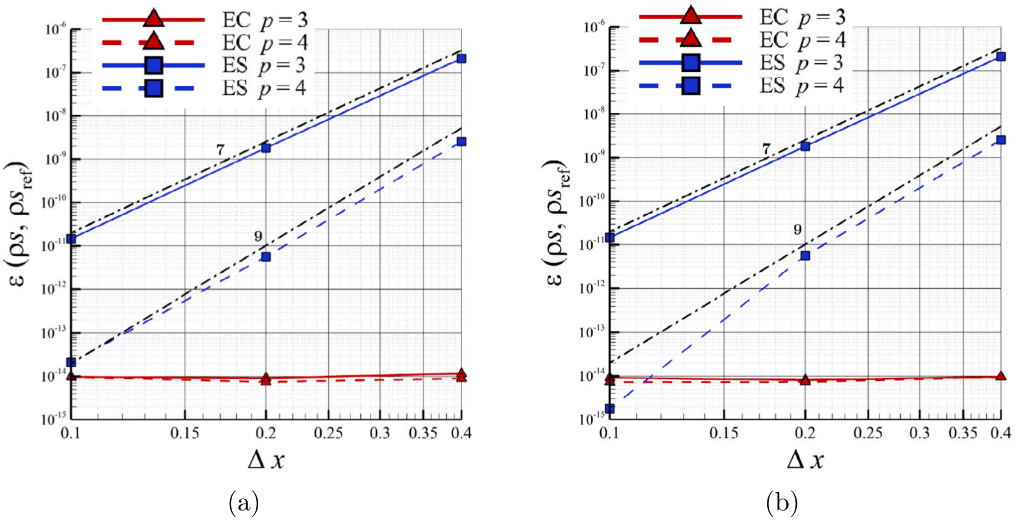

(a)

(b)

Fig. 2. IVC — spatial refinement test. Errors ε on the entropy. Simulations integrated in time via the explicit SSPRK35. (a) DEEB$_b$ and (b) strong-form pressure modification.

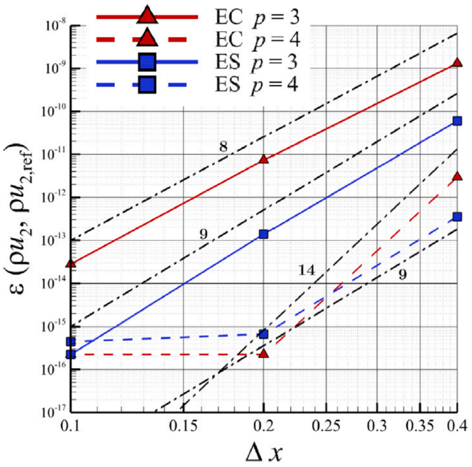

Fig. 3. IVC — spatial refinement test. Errors ε on the momentum component ρu_2 for the strong-form pressure modification. Simulations integrated in time via the explicit SSPRK35.

that exactly conserves entropy once the flux of [17] is chosen. Clearly, the pressure-based strategy significantly differs from the various DEEB corrections, because it equates to introducing a modification in the discretization strategy that prioritizes entropy conservation over momentum. The latter is in fact unavoidably spoiled as displayed by the conservation error of Fig. 3, although it is at least $\mathcal{O}(h_K^{2p+d})$, like the α_k integration error.

3.1.2. Robustness

The robustness of the different formulations is assessed by considering their performance on challenging flow problems. The case studies are chosen in such a way to combine under-resolution and highly energetic phenomena. Specifically, the flows taken into account are the Kelvin–Helmholtz and the Richtmyer–Meshkov instability. Due to the hard numerical challenge posed by the two test cases, the convective terms are discretized by means of the ES Godunov flux. Similarly to what was done in [2], the robustness of the methods is quantified by means of the completion index

$$\mathrm{CI} = \frac{\sum_{j=1}^{N_{tot}} (t_{end})_j}{N_{tot}\, t_f}, \tag{53}$$

identifying the ratio between the cumulative simulated time over a range of N_{tot} numerical runs and the total time corresponding to the successful completion of all tests up to the chosen end time t_f. Since the pressure-based entropy correction is denoted by a poor robustness even when compared to the STD strategy, we do not include its results. We would also like to premise that the STD entropy projection formulation is significantly more robust than the standard conservative formulation, which is able to complete the following tests only up to $p = 1$, see [2] for the detailed comparison.

The Kelvin–Helmholtz instability. In a compressible framework, the Kelvin–Helmholtz instability (KHI) arises from a momentum stratification superimposed to a density gradient. The Atwood number $A = (\rho_2 - \rho_1)/(\rho_1 + \rho_2) \in [0, 1)$ is the parameter commonly used to quantify the instability driving force, providing a measure of the starting density gradient. The higher the Atwood number the more critical the instability; as the density ratio increases ρ assumes progressively smaller values in the low-density region of the domain, eventually resulting in a local speed of sound $\sqrt{\gamma P/\rho}$ that leads to supersonic Mach numbers as soon as $A = 0.75$. Following [1], the initial condition is defined as

$$\begin{aligned}
u_1 &= \left(f(x_2) - \frac{1}{2} \right),\\
u_2 &= \frac{1}{10}\sin(2\pi x_1),\\
P &= 1,\\
\rho &= \rho_1 + f(x_2)\left(\rho_2 - \rho_1\right),
\end{aligned} \tag{54}$$

where $\rho_1 = 1$ and $f(x_2) = (1/2)[\tanh(15x_2 + 7.5) - \tanh(15x_2 - 7.5)]$ is a smoothing function. The solution is integrated in time up to $t_f = 14$ on a doubly periodic square domain of size $[-1, 1]^2$, discretized with Cartesian grids (*rect*) made of $2^4{\times}2^4$ (*coarse*) and $2^5{\times}2^5$ (*fine*) elements. The same subdivisions are also used to construct meshes made of triangular elements (*tri*), in order to evaluate the effect of different cell shapes. The robustness of the different solution strategies is tested for $A = 0.75$, using DG approximations of degree $p = \{4, \dots, 7\}$.

The results in terms of CI are depicted in Fig. 4 for all the grids and entropy correction strategies investigated, where it is also possible to identify the effect of retaining α_K only when it contributes to the increase of physical entropy. Overall we note that, irrespective of how the correction is distributed across the residual DoF, the DEEB always guarantees a robustness improvement over the baseline STD strategy. Furthermore, a distinct effect regarding $\alpha_K \geq 0$ may be identified only for the (viscous-like) DEEB$_b$ strategy in the *fine* grids. One can also note that DEEB$_b$ as well as DEEB$_a$ appear to be more robust than the other strategies in case of triangular grids. In this respect, the *fine* discretizations based on triangular elements pose a notable robustness challenge for this case, as all schemes exhibit a significantly lower CI compared to the values observed with rectangular grids. However, it should be pointed out that these tests are focused on high-order discretizations, with $p \geq 4$, and in fact we verified that while all DEEB variants complete the simulations on the *fine* triangular grids up to $p = 3$, STD fails for $p > 1$.

In Fig. 5 we display the instantaneous contours of the density ρ for the two strategies DEEB$_a$ and DEEB$_b$ with and without the control over the introduction of α_K depending on its sign. Since we are dealing with a structurally under-resolved problem [1,39], the final solution is strongly dependent on the discretization, as evidenced by the distinct solutions derived for each numerical configuration.

Finally, in Table 2 we report the increment in CPU time of the different DEEB implementations with respect to DEEB$_{std}$. All data refer to a complete run, up to simulation end-time t_f. We note that although the measured simulation time includes the contribution of I/O operations, for the considered long-run simulations this accounts for only a fraction of the time dedicated to the actual solution procedure. Hence, since the numerical runs only differ in the operations performed to distribute the correction α_K, the reported times provide a reasonably accurate evaluation of the computational efficiency of the different schemes. The simulations are performed using two nodes of a cluster mounting two Intel Xeon CPU E5-2620 v4 with eight cores each for a total of thirty two MPI threads.

It is easy to see that the need to perform additional integration loops introduces a computational overhead that can translate in slowdown of up to a 50%. In this sense, we note that the orthonormality of our basis may be leveraged to avoid explicit quadrature loops also for the DEEB$_c$ implementation, therefore it is expected that a more efficient coding could reduce its computational cost.

The Richtmyer–Meshkov instability. The Richtmyer–Meshkov Instability (RMI) [40,41] is a flow phenomenon characterized by a shock wave traveling through a stratified fluid. The flow is initialized as

$$\begin{aligned}
u_i &= 0,\\
P &= 4.9 - 1.95\left[1 + \tanh\left(2\xi_1\right)\right],\\
\rho &= 4.22 - 1.985\left[2 + \tanh\left(2\xi_1\right) + \tanh\left(2\xi_2\right)\right],
\end{aligned} \tag{55}$$

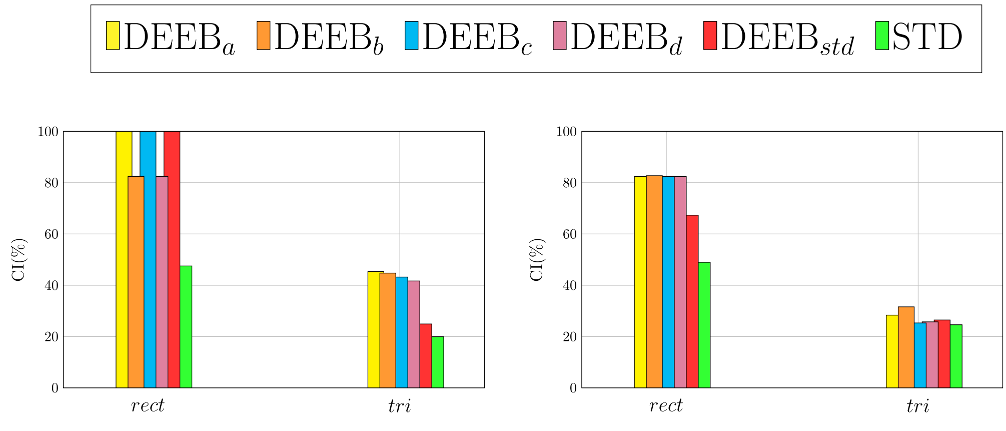

(a) $2^4 \times 2^4$ grid, $\alpha_K \geq 0$

(b) $2^5 \times 2^5$ grid, $\alpha_K \geq 0$

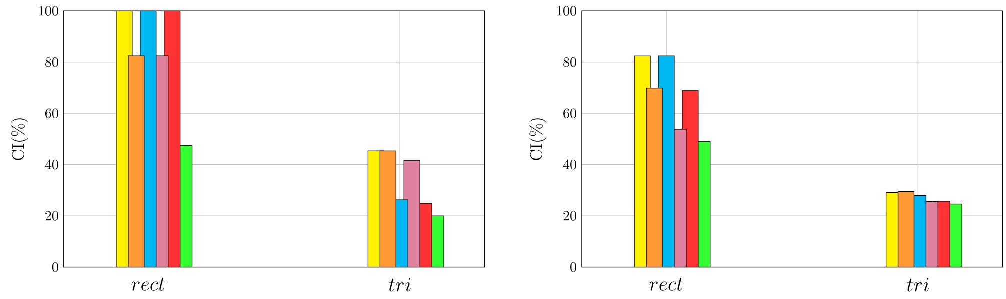

(c) $2^4 \times 2^4$ grid, $\alpha_K \lesseqgtr 0$

(d) $2^5 \times 2^5$ grid, $\alpha_K \lesseqgtr 0$

Fig. 4. KHI, $A = 0.75$ - bar charts for comparing the robustness of the various DEEB spreading term variants. The completion index covers the range $p = \{4, \ldots, 7\}$.

Table 2
KHI, $A = 0.33$ — Ratio between the CPU time of the alternative DEEB variants and the standard one. Computations performed on the Cartesian grid $2^5 \times 2^5$ over the polynomial range $p = \{3, \ldots, 7\}$.

$\frac{\text{CPU}_{\text{time}}(\circ)}{\text{CPU}_{\text{time}}(Std)}$	p				
	3	4	5	6	7
DEEB$_a$	1.2	1.2	1.2	1.3	1.3
DEEB$_b$	1.4	1.3	1.4	1.4	1.5
DEEB$_c$	1.3	1.3	1.2	1.3	1.3
DEEB$_d$	1.2	1.3	1.2	1.3	1.3

where

$$
\begin{aligned}
\xi_1 &= |x_2 - 4| - 2, \\
\xi_2 &= x_2 - \left[18 + 2\cos(6\pi x_1/40)\right].
\end{aligned}
\tag{56}
$$

Although the original fluid domain is a $[0, 40/3] \times [0, 40]$ rectangle, in this work simulations are run on half of it, i.e. $x_1 \in [0, 40/6]$, imposing symmetric boundary conditions on one side to save computational time. The halved domain is discretized with a 8×48 (*coarse*) and a 16×96 (*fine*) grid, both composed by quadrilateral and triangular elements as in the previous test case. All computations are performed integrating the solution in time up to $t_f = 42$.

In Fig. 6 we illustrate the results obtained in terms of CI for the different DEEB strategies, further discriminating the variant that adds the correction regardless the sign of α_K and the one in which the solution is corrected only if α_K is positive. Particularly, in the latter variant we note that the DEEB$_a$ strategy is able to complete all the simulations, see Figs. 6(a) and 6(b). Likewise, retaining the entropy correction only if $\alpha_K \geq 0$ appears to be substantially advantageous also for DEEB$_b$ as it exhibits just an isolated crash at $p = 6$. In contrast, if the correction is distributed regardless of the sign of α_K the same strategies are subjected to a remarkable decrease in robustness, since they maintain the maximum CI only for the *coarse* triangular discretization. The remaining DEEB implementations, instead, do not exhibit a particular sensitivity to the sign of the committed entropy error, with no sensible variation that may be appreciated in their CI across the outlined configurations. In any case, it is worth highlighting that even for the RMI the baseline STD approach emerges as the least stable, especially in the simulations performed on triangular grids.

Lastly, in Fig. 7 we depict the instantaneous density contours at t_f for the DEEB$_a$ and DEEB$_b$ strategies on the *fine* Cartesian and the triangular meshes. The solutions obtained on the triangular grid are reflected on the $x_1 = 40/6$ axis. Analogously to KHI, also RMI exhibits a structural under-resolution which is now coupled with sharp gradients in all flow variables due to the development of flow discontinuities, i.e. shock waves. In this sense, the robustness is further stressed by the absence of any control over the oscillations of the solution (e.g. shock capturing). This may be clearly observed by looking at the high density region at the bottom of Figs. 7(a) and 7(b). What may be appreciated is the strong dependence of the solution on the adopted spatial discretization. Indeed, although some differences may be visible between the two DEEB strategies, the most significant variation of the solution is obtained switching from a Cartesian to a triangular grid.

3.2. *Results of the viscous test cases*

In Section 2.1.2 it is observed that for a strictly entropy stable behavior of the BR discretizations the viscous fluxes ought to live in the polynomial space of the DG solution. However, since the projected entropy state $\mathbf{v}_h$ is used in the construction of the discrete spatial op-

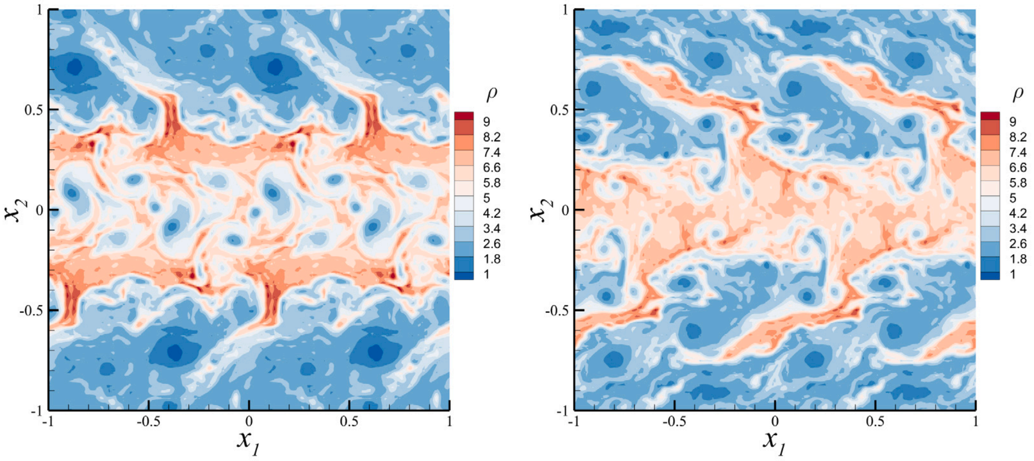

(a) DEEB$_a$, $\alpha_K \lessgtr 0$ (b) DEEB$_b$, $\alpha_K \lessgtr 0$

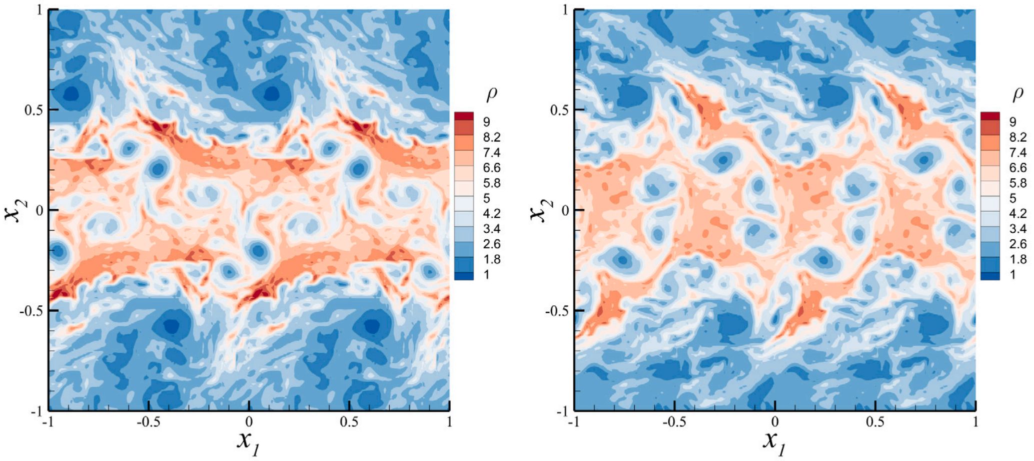

(c) DEEB$_a$, $\alpha_K \geq 0$ (d) DEEB$_b$, $\alpha_K \geq 0$

Fig. 5. KHI, $A = 0.75$ - density contours at time t_f. Solutions portrayed at $p = 6$ for the *fine* Cartesian mesh $2^5 \times 2^5$.

erators, the matrix $\mathbf{K}(\mathbf{v}_h)$ presents entries which are rational functions. To obviate this and secure the discrete entropy stability of the viscous term, we introduce for the latter an additional L_2-projection onto the polynomial solution space.

For the sake of completeness, we also remark that the schemes employ an entropy stable discretization of the convective terms. This, particularly, is obtained by combining the entropy correction implemented as DEEB$_{std}$ with an interface convective flux computed via the exact Riemann solver of [38].

3.2.1. Convergence

To demonstrate that the projection error introduced in this scenario does not alter the order of accuracy of the scheme, a convergence analysis based on the Method of Manufactured Solutions [42] is performed. In such approach, an analytical solution is decided a priori and a source term is added to the discretization, based on the discrete operators computed according to the desired final state. Afterwards, the accuracy is assessed through the behavior of the error between the preselected analytical solution and the discrete one for increasing spatial refinements. In all simulations the CFL is set to $5 \cdot 10^{-2}$.

In our case, the mathematical form of the steady-state solution expressed in primitive variables $[\rho, \mathbf{u}, P]^\top$ and SI units is defined as

$$\psi(x_1, x_2) = \mathtt{a}_0^\psi + \mathtt{a}_1^\psi\,\mathtt{f}_1\left(\mathtt{b}_1^\psi\,\frac{x_1}{L}\pi\right) + \mathtt{a}_2^\psi\,\mathtt{f}_2\left(\mathtt{b}_2^\psi\,\frac{x_2}{L}\pi\right) + \mathtt{a}_{1,2}^\psi\,\mathtt{f}_{1,2}\left(\mathtt{b}_{1,2}^\psi\,\frac{x_1 x_2}{L^2}\pi\right), \tag{57}$$

where constants and trigonometric functions are set according to [42] and reported in Table 3. Note that each $\mathtt{a}^\psi$ constant has the same dimensions as the corresponding primitive variable, while the $\mathtt{b}^\psi$ coefficients are dimensionless.

As far as the computational setup is concerned, the discrete solution is computed on a square domain $\Omega = [0, L]^2$, where $L = 1\,\mathrm{m}$. The gas properties are identified by $R = 287\,\mathrm{J/(kg\,K)}$ and $\gamma = 1.4$. The Reynolds number is $Re = a_0^\rho c L/\mu = 100$, with $c = \sqrt{\gamma a_0^P / a_0^\rho}$, while the Prandtl number and the power-law coefficient of Eq. (3) are set to $\Pr = 0.72$ and $\beta = 0.75$, respectively. The spatial convergence test is performed for the polynomial degrees $p = \{1, \dots, 6\}$ on a set of progressively finer uniform meshes made of $2^i \times 2^i$ quadrilateral elements, where $i = 1, \dots, 4$.

Fig. 8 portrays the convergence result for the standard BR1 and BR2 schemes together with their projected counterparts, i.e. Π_{BR1} and

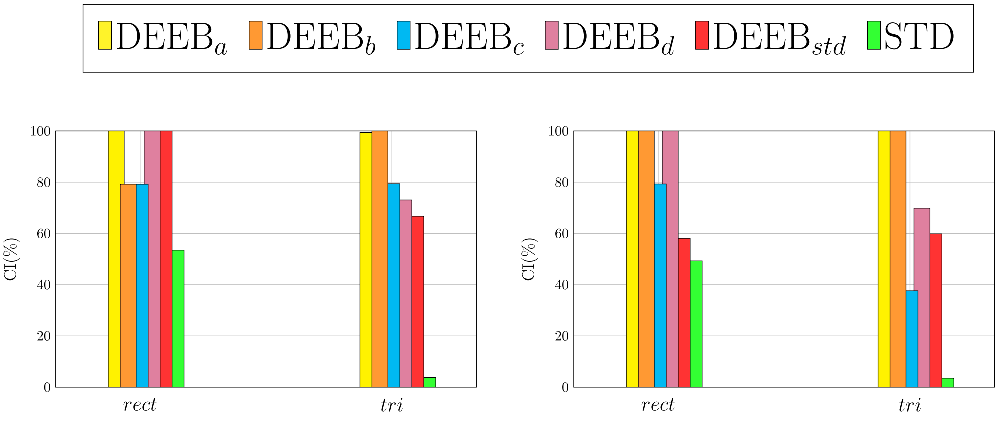

(a) 8 × 48 grid, $\alpha_K \geq 0$ (b) 16 × 96 grid, $\alpha_K \geq 0$

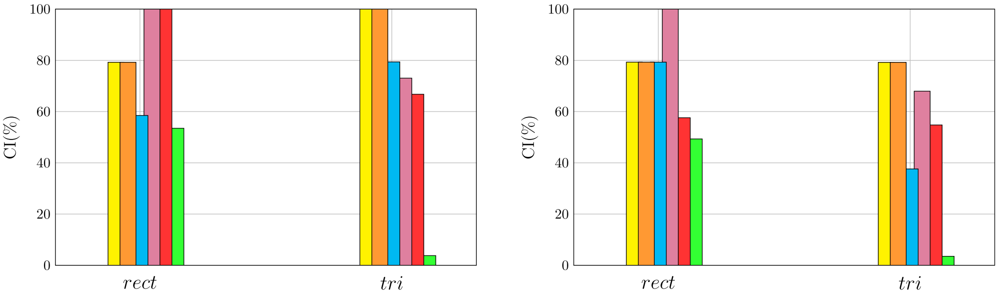

(c) 8 × 48 grid, $\alpha_K \lessgtr 0$ (d) 16 × 96 grid, $\alpha_K \lessgtr 0$

Fig. 6. RMI — bar charts for comparing the robustness of the various DEEB spreading term variants. The completion index covers the range $p = \{4, \ldots, 7\}$.

Table 3
Spatial convergence test —- constants and trigonometric functions for the primitive variable of the subsonic manufactured solution for the Navier–Stokes equations. Each $\mathtt{a}^\psi$ constant (SI units) has the same dimensions as the corresponding primitive variable, while the $\mathtt{b}^\psi$ coefficients are dimensionless.

ψ	$\mathtt{a}_0^\psi$	$\mathtt{a}_1^\psi$	$\mathtt{a}_2^\psi$	$\mathtt{a}_{1,2}^\psi$	$\mathtt{f}_1^\psi$	$\mathtt{f}_2^\psi$	$\mathtt{f}_{1,2}^\psi$	$\mathtt{b}_1^\psi$	$\mathtt{b}_2^\psi$	$\mathtt{b}_{1,2}^\psi$
ρ	1	0.1	0.15	0.08	sin	cos	cos	0.75	1.0	1.25
u	70	4	−12	7	sin	cos	cos	5.13	1.5	0.6
v	90	−20	4	−11	cos	sin	cos	1.5	1.0	0.9
P	100 000	−30 000	20 000	−25 000	cos	sin	sin	1.0	1.25	0.75

Π_{BR2}. It may be observed that using the L_2-projection of the viscous flux in the computation of the diffusive discrete operator does not alter the order of accuracy of the scheme, which remains $p + 1$.

3.2.2. Robustness

In order to evaluate the potential improvement in robustness owed to the entropy stable implementation of the two viscous discretization schemes, i.e. Π_{BR1} and Π_{BR2}, the same tests run in Section 3.1.2 are performed on the viscous extension of the KHI. The computations are carried out on the coarse rectilinear mesh $2^4 \times 2^4$ illustrated in Section 3.1.1 and with a small CFL number, i.e. $5 \cdot 10^{-3}$, to highlight as much as possible the sole effect of the spatial discretizations. The end time for the simulations is set to $t_f = 10/\sqrt{\gamma}$. Since the viscosity makes the under-resolution challenge less problematic in the KHI flow due to the introduction of a non-zero cutoff for the length scales, we test the entropy stable discrete viscous frameworks with a very large Atwood number, i.e. $A = 0.99$; this means initializing the double shear layer with a density stratification ratio $\rho_2/\rho_1 = 199$. Given that the reference pressure is set to 1 as well the reference density, ρ_1, such configuration creates a low-temperature bulk flow containing most of the total mass which, being initialized under strongly supersonic conditions and with small viscosity effects, behaves almost as an inviscid field. On the other hand, at the interface between the bulk and the outer layers, where very large velocity gradients exist, viscous stresses dominate the flow dynamics. Regarding the Reynolds number, its value is set in relation to the speed of sound $\sqrt{\gamma P/\rho_1}$, hence $\mu_1 = \sqrt{\gamma} Re^{-1}$. In the bulk, instead, the viscosity becomes $\mu_2 = \sqrt{\gamma} Re^{-1} \rho_2^{-\beta}$ in accordance with Eq. (3), where $\mu_{ref} = \mu_1$.

In the first set of simulations, performed at $Re = 100$ and $\beta = 3/4$, the projection of the viscous terms of Eq. (39) takes into consideration a strong variation of viscosity, having $\mu_2 \simeq 0.02\mu_1$. Fig. 9 reports the temporal variation of the total thermodynamic entropy for the different schemes, monitored according to the metric $\varepsilon(\circ, \bullet_{ref})$ outlined in Section 3.1.1. Notably, only the Π_{BR2} scheme is able to run at polynomial order up to $p = 3$ until the end time. It is also interesting to observe that this variant, which is the most robust of those considered, produces the least amount of numerical entropy within the time window completed by all the schemes. As expected, this behavior confirms that all discretizations of the viscous terms considered so far generally produce an increase in total physical entropy. However, only the Π_{BR1} and Π_{BR2} schemes are characterized by a fine local control of the physical entropy production. In other words, a globally increasing ρs by itself is not enough to guarantee a consistent evolution of the physical entropy in all the mesh elements. Moreover, it is worth underlining that for Π_{BR2} a threshold value may be identified for the penalization coefficient η_F, in fact for $\eta_F < 2$ the scheme is not able to run the simulation to completion. This result is consistent with Eq. (42) which shows how a larger η_F increases the entropy stability. Oppositely, Eq. (47) ensures entropy stability but in a somehow relaxed version and there is no parameter to tune the production of the thermodynamic entropy. As a result, the scheme crashes at $p = 3$ along with the standard

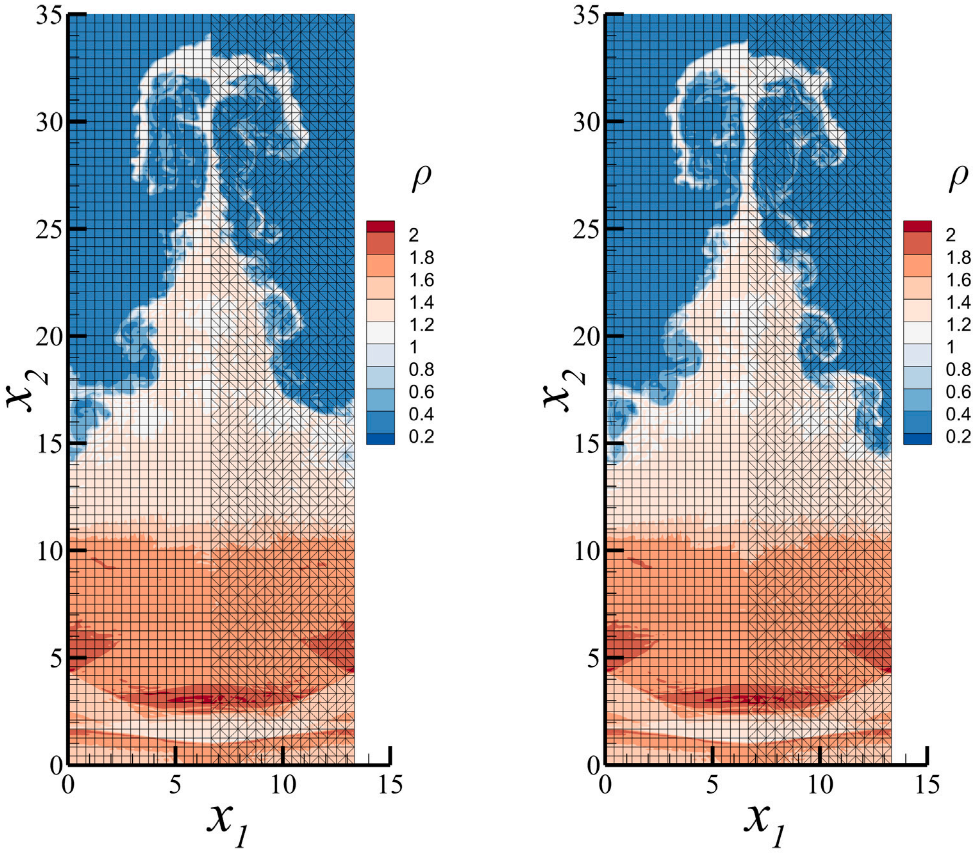

(a) DEEB$_a$ (b) DEEB$_b$

Fig. 7. RMI — density contours at time t_f. Solutions portrayed at $p = 7$ for the *fine* Cartesian and triangular meshes.

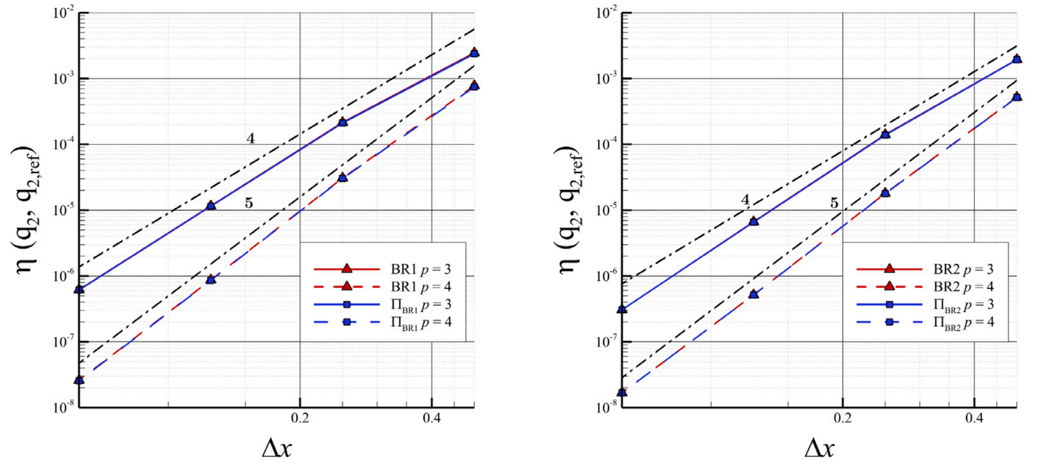

(a)   (b)

Fig. 8. Spatial convergence test for (a) BR1, Π_{BR1} and (b) BR2, Π_{BR2} schemes — subsonic manufactured solution for the Navier–Stokes equations at $Re = 100$.

non-projected variants. Fig. 10 portrays the end time solution for the Π_{BR2} scheme, in terms of Mach number and viscosity field. Since the temperature reaches very low values in a significant portion of the domain, most of the flow experiences a strongly supersonic regime. In the second set of simulations, to avoid a strict coupling of the local viscosity with the temperature, the power law coefficient $\beta = 0$ is used. Therefore, $\mu = \sqrt{\gamma}Re^{-1}$ is set everywhere. It is observed that whilst at polynomial order $p = 3$ all schemes are able to reach the end time for $Re < 500$, for $Re = 500$ only the Π_{BR2} scheme successfully completes the numerical run, see Fig. 11, while Fig. 12 reports a snapshot of the final flow field. These results prove that the case with $\beta = 0$ is less demanding, since the viscous projection only considers the variation of the thermodynamic state in the matrices $\mathbf{K}_{i,j}(\mathbf{v}_h)$ of the Appendix and not the viscosity gradient. Moreover, the threshold value for the

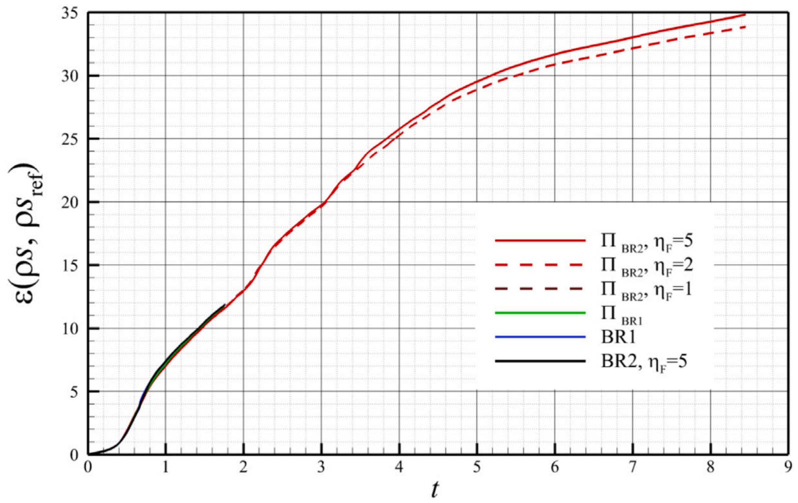

Fig. 9. Comparison of the viscous discretization schemes in terms of time variation of the total entropy for the viscous KHI at $A = 0.99$, $Re = 100$ and $\beta = 0.75$, with $p = 3$.

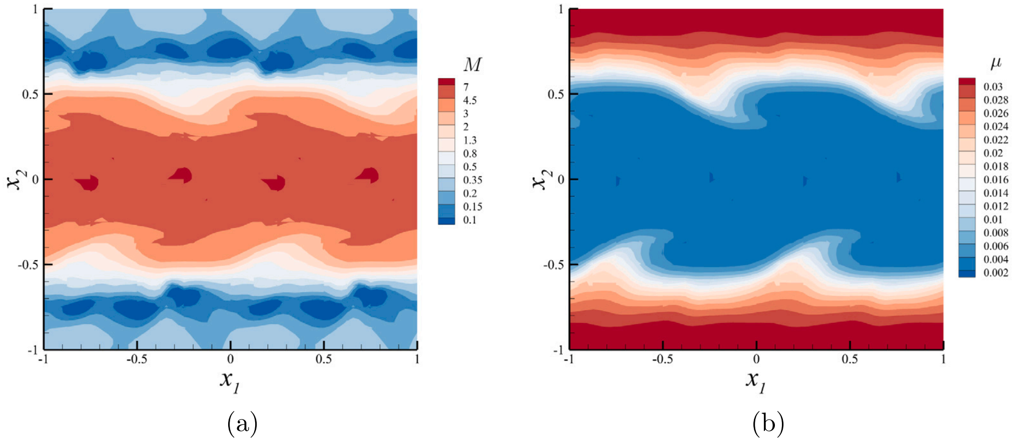

(a)

(b)

Fig. 10. Viscous KHI at $A = 0.99$, $Re = 100$, $\beta = 0.75$, with $p = 3$, for the Π_{BR2} scheme with $\eta_F = 5$. Contours at t_f of (a) Mach number and (b) dynamic viscosity.

Table 4
Viscous KHI, $A = 0.95$ — Ratio between the CPU time of the BR2 viscous discretization and its projected counterpart. Computations performed on a $2^4 \times 2^4$ Cartesian grid over the polynomial range $p = \{3, \dots, 7\}$.

$\frac{\mathrm{CPU}_{\mathrm{time}}(\Pi_{BR2})}{\mathrm{CPU}_{\mathrm{time}}(BR2)}$	p				
	3	4	5	6	7
Π_{BR2}	1.34	1.42	1.52	1.58	1.62

penalty factor so as to avoid the blow up of the simulation is $\eta_F = 4$, considerably closer to the theoretical stability value $card(\mathcal{F}_K) + 1$ with respect to the previous case.

Although Π_{BR2} produces an improvement in robustness for some configurations, it also causes a significant increase in computational cost. This overhead, depicted in Table 4, clearly arises from the additional integrals required for the projection operation, which poorly scales with the adopted polynomial approximation order, and the associated parallel communications demand. Also in this case, similar to what is reported for inviscid calculations, the CPU times refer to complete calculations up to the simulation end time t_f.

4. Conclusion

This paper presents a high-order modal DG numerical framework ensuring a fully entropy stable discretization of the Navier–Stokes equations. A physically compatible evolution of the numerical entropy is achieved by leveraging the entropy projection–correction approach outlined in [2]. To further enforce entropy stability on the discrete viscous operator, an additional L_2-projection of the viscous fluxes is introduced, a necessity justified by the fact that the lift operators of the Bassi–Rebay viscous schemes are strictly defined across polynomial spaces. We investigate several alternative strategies for the distribution of the correction, showing that all DEEB formulations guarantee a significant robustness improvement over the baseline algorithm. In particular, we note that the implementations referred to as DEEB$_a$, DEEB$_b$ and DEEB$_c$ ensure the largest robustness enhancement among the considered strategies. Despite this, DEEB$_{std}$ remains the strategy with the highest computational efficiency thanks to the orthonormality of the basis functions adopted. On a similar note, we show that the entropy stable Π_{BR2} implementation of the BR2 scheme offers some advantages in terms of robustness when considering the viscous KHI case at an extremely high Atwood number, i.e. $A = 0.99$. Nevertheless, the projection operation introduces a significant computational overhead

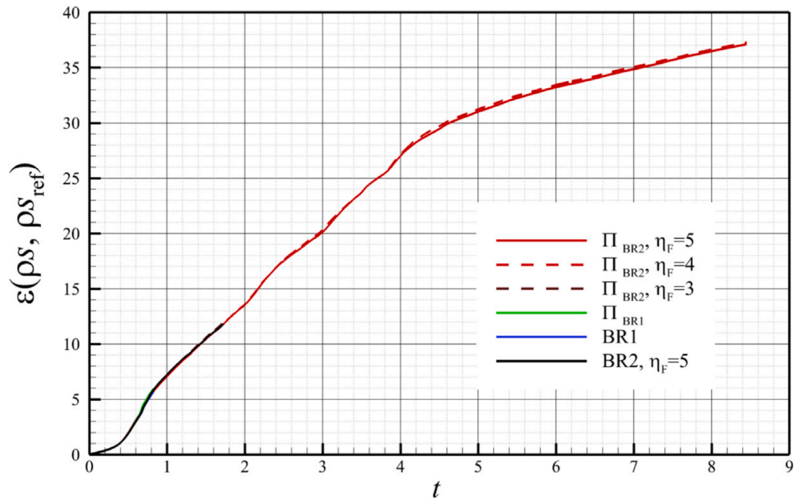

Fig. 11. Comparison of the viscous discretization schemes in terms of time variation of the total entropy for the viscous KHI at $A = 0.99$, $Re = 500$ and $\beta = 0$, with $p = 3$.

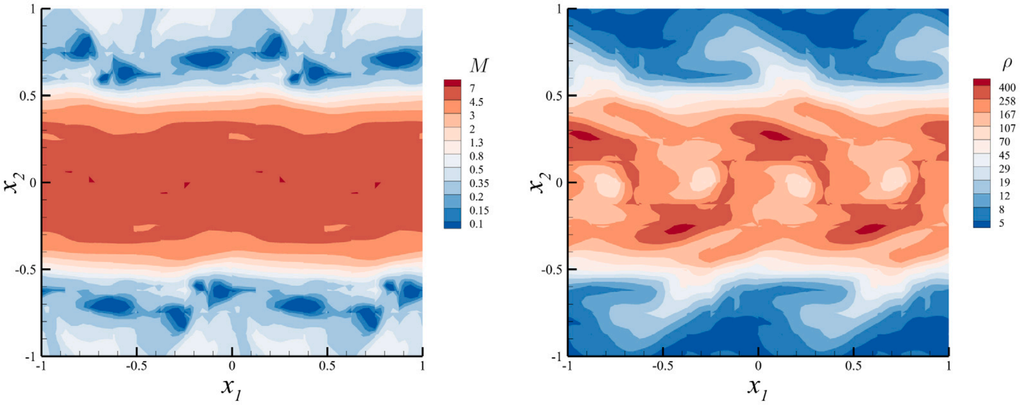

(a)

(b)

Fig. 12. Viscous KHI at $A = 0.99$, $Re = 500$, $\beta = 0$, with $p = 3$, for the Π_{BR2} scheme with $\eta_F = 5$. Contours at t_f of (a) Mach number and (b) density.

that, at this stage, tends to hinder its applicability in production-grade solvers.

CRediT authorship contribution statement

Luca Alberti: Writing – review & editing, Visualization, Validation, Software, Methodology, Investigation, Formal analysis, Data curation. **Emanuele Carnevali:** Writing – original draft, Visualization, Validation, Software, Methodology, Investigation, Formal analysis, Data curation, Conceptualization. **Alessandro Colombo:** Writing – original draft, Software, Formal analysis, Conceptualization. **Andrea Crivellini:** Writing – review & editing, Validation, Supervision, Software, Resources, Methodology, Investigation, Formal analysis, Data curation, Conceptualization.

Declaration of competing interest

The authors declare that they have no known competing financial interests or personal relationships that could have appeared to influence the work reported in this paper.

Appendix. Symmetrized matrices for the viscous fluxes

The matrices $\mathbf{K}_{i,j}(\mathbf{v})$ appearing in the viscous flux definition of Eq. (10) denote the blocks of the symmetric and positive semi-definite matrix

$$\mathbf{K}(\mathbf{v}) = \begin{bmatrix} \mathbf{K}_{1,1}(\mathbf{v}) & \dots & \mathbf{K}_{1,d}(\mathbf{v}) \\ \vdots & \ddots & \vdots \\ \mathbf{K}_{d,1}(\mathbf{v}) & \dots & \mathbf{K}_{d,d}(\mathbf{v}) \end{bmatrix} = \mathbf{K}(\mathbf{v})^{\top} \quad | \quad \mathbf{x}^{\top}\mathbf{K}(\mathbf{v})\mathbf{x} \geq 0 \quad \forall \mathbf{x} \in \mathbb{R}^{d(d+2)}. \tag{A.1}$$

The coefficients of $\mathbf{K}_{i,j}(\mathbf{v})$ are here reported for the sake of completeness (see Eqs. (A.2)–(A.7))

$$\mathbf{K}_{1,2} = \frac{1}{\mathrm{v}_5^3} \begin{bmatrix} 0 & 0 & 0 & 0 & 0 \\ 0 & 0 & -\lambda \mathrm{v}_5^2 & 0 & \lambda \beta_2 \\ 0 & -\mu \mathrm{v}_5^2 & 0 & 0 & \mu \beta_1 \\ 0 & 0 & 0 & 0 & 0 \\ 0 & \mu \beta_2 & \lambda \beta_1 & 0 & (\lambda + \mu)\alpha_1 \end{bmatrix}, \tag{A.2}$$

$$\mathbf{K}_{1,1} = \frac{1}{\mathrm{v}_5^3}\begin{bmatrix} 0 & 0 & 0 & 0 & 0 \\ 0 & -(\lambda+2\mu)\mathrm{v}_5^2 & 0 & 0 & (\lambda+2\mu)\beta_1 \\ 0 & 0 & -\mu\mathrm{v}_5^2 & 0 & \mu\beta_2 \\ 0 & 0 & 0 & -\mu\mathrm{v}_5^2 & \mu\beta_3 \\ 0 & (\lambda+2\mu)\beta_1 & \mu\beta_2 & \mu\beta_3 & -\left[(\lambda+2\mu)V_2^2+\mu\left(\mathrm{v}_3^2+\mathrm{v}_4^2\right)-\gamma\mu\mathrm{v}_5/Pr\right] \end{bmatrix}, \tag{A.3}$$

$$\mathbf{K}_{2,2} = \frac{1}{\mathrm{v}_5^3}\begin{bmatrix} 0 & 0 & 0 & 0 & 0 \\ 0 & -\mu\mathrm{v}_5^2 & 0 & 0 & \mu\beta_1 \\ 0 & 0 & -(\lambda+2\mu)\mathrm{v}_5^2 & 0 & (\lambda+2\mu)\beta_2 \\ 0 & 0 & 0 & -\mu\mathrm{v}_5^2 & \mu\beta_3 \\ 0 & \mu\beta_1 & (\lambda+2\mu)\beta_2 & \mu\beta_3 & -\left[(\lambda+2\mu)\mathrm{v}_3^2+\mu\left(\mathrm{v}_2^2+\mathrm{v}_4^2\right)-\gamma\mu\mathrm{v}_5/Pr\right] \end{bmatrix}, \tag{A.4}$$

$$\mathbf{K}_{3,3} = \frac{1}{\mathrm{v}_5^3}\begin{bmatrix} 0 & 0 & 0 & 0 & 0 \\ 0 & -\mu\mathrm{v}_5^2 & 0 & 0 & \mu\beta_1 \\ 0 & 0 & -\mu\mathrm{v}_5^2 & 0 & \mu\beta_2 \\ 0 & 0 & 0 & -(\lambda+2\mu)\mathrm{v}_5^2 & (\lambda+2\mu)\beta_3 \\ 0 & \mu\beta_1 & \mu\beta_2 & (\lambda+2\mu)\beta_3 & -\left[(\lambda+2\mu)\mathrm{v}_4^2+\mu\left(\mathrm{v}_2^2+\mathrm{v}_3^2\right)-\gamma\mu\mathrm{v}_5/Pr\right] \end{bmatrix}, \tag{A.5}$$

Box I.

$$\mathbf{K}_{1,3} = \frac{1}{\mathrm{v}_5^3}\begin{bmatrix} 0 & 0 & 0 & 0 & 0 \\ 0 & 0 & 0 & -\lambda\mathrm{v}_5^2 & \lambda\beta_3 \\ 0 & 0 & 0 & 0 & 0 \\ 0 & -\mu\mathrm{v}_5^2 & 0 & 0 & \mu\beta_1 \\ 0 & \mu\beta_3 & 0 & \lambda\beta_1 & (\lambda+\mu)\alpha_2 \end{bmatrix}, \tag{A.6}$$

$$\mathbf{K}_{2,3} = \frac{1}{\mathrm{v}_5^3}\begin{bmatrix} 0 & 0 & 0 & 0 & 0 \\ 0 & 0 & 0 & 0 & 0 \\ 0 & 0 & 0 & -\lambda\mathrm{v}_5^2 & \lambda\beta_3 \\ 0 & 0 & -\mu\mathrm{v}_5^2 & 0 & \mu\beta_2 \\ 0 & 0 & \mu\beta_3 & \lambda\beta_2 & (\lambda+\mu)\alpha_3 \end{bmatrix}. \tag{A.7}$$

where

$$\alpha_1 = -\mathrm{v}_2\mathrm{v}_3, \quad \alpha_2 = -\mathrm{v}_2\mathrm{v}_4, \quad \alpha_3 = -\mathrm{v}_3\mathrm{v}_4 \tag{A.8}$$

and

$$\beta_1 = \mathrm{v}_2\mathrm{v}_5, \quad \beta_2 = \mathrm{v}_3\mathrm{v}_5, \quad \beta_3 = \mathrm{v}_4\mathrm{v}_5. \tag{A.9}$$

From the previous expression it is immediate to find the definition of $\mathbf{K}^*_{i,j}(\mathbf{v}) = \mu^{-1}\mathbf{K}_{i,j}(\mathbf{v})$ once a specific λ is chosen. We recall that in this work we set $\lambda = -2/3\mu$. Actually, the DEEB$_b$ approach also requires a Prandtl number even in the inviscid case, which is somewhat arbitrary. In our case, particularly, we decided to select $Pr = 0.72$.

Data availability

Data will be made available on request.

References

[1] Chan J, Ranocha H, Rueda-Ramírez AM, Gassner G, Warburton T. On the entropy projection and the robustness of high order entropy stable discontinuous Galerkin schemes for under-resolved flows. Front Phys 2022;356.

[2] Alberti L, Carnevali E, Colombo A, Crivellini A. An entropy conserving/stable discontinuous Galerkin solver in entropy variables based on the direct enforcement of entropy balance. J Comput Phys 2024;508.

[3] Gassner GJ, Winters AR, Kopriva DA. Split form nodal discontinuous Galerkin schemes with summation-by-parts property for the compressible Euler equations. J Comput Phys 2016;327:39–66.

[4] Fisher TC, Carpenter MH. High-order entropy stable finite difference schemes for nonlinear conservation laws: Finite domains. J Comput Phys 2013;252:518–57.

[5] Gassner GJ. A skew-symmetric discontinuous Galerkin spectral element discretization and its relation to SBP-SAT finite difference methods. SIAM J Sci Comput 2013;35(3):A1233–53.

[6] Carpenter M, Fisher T, Nielsen E, Parsani M, Svärd M, Yamaleev N. Entropy stable summation-by-parts formulations for compressible computational fluid dynamics. In: Handbook of numerical analysis. vol. 17, Elsevier; 2016, p. 495–524.

[7] Chan J. On discretely entropy conservative and entropy stable discontinuous Galerkin methods. J Comput Phys 2018;362:346–74.

[8] Chen T, Shu C-W. Review of entropy stable discontinuous Galerkin methods for systems of conservation laws on unstructured simplex meshes. CSIAM Trans Appl Math 2020;1(1):1–52.

[9] Renac F. Entropy stable, robust and high-order DGSEM for the compressible multicomponent Euler equations. J Comput Phys 2021;445:110584.

[10] Abgrall R. A general framework to construct schemes satisfying additional conservation relations. Application to entropy conservative and entropy dissipative schemes. J Comput Phys 2018;372:640–66.

[11] Alberti L, Bassi F, Carnevali E, Colombo A, Crivellini A, Nigro A. A comparative study of different sets of variables in a discontinuous Galerkin method with entropy balance enforcement. Int J Comput Fluid Dyn 2023;37(6):487–508.

[12] Tadmor E. Entropy stability theory for difference approximations of nonlinear conservation laws and related time-dependent problems. Acta Numer 2003;12:451–512.

[13] Brezzi F, Manzini G, Marini D, Pietra P, Russo A. Discontinuous Galerkin approximations for elliptic problems. Numer Methods Partial Differential Equations 2000;16(4):365–78.

[14] Bassi F, Rebay S. High–order accurate discontinuous finite element solution of the 2D Euler equations. J Comput Phys 1997;138(2):251–85.

[15] Bassi F, Botti L, Colombo A, Di Pietro DA, Tesini P. On the flexibility of agglomeration based physical space discontinuous Galerkin discretizations. J Comput Phys 2012;231(1):45–65.

[16] Hughes TJ, Franca LP, Mallet M. A new finite element formulation for computational fluid dynamics: I. symmetric forms of the compressible Euler and Navier-Stokes equations and the second law of thermodynamics. Comput Methods Appl Mech Engrg 1986;54(2):223–34.

[17] Ismail F, Roe PL. Affordable, entropy-consistent Euler flux functions II: Entropy production at shocks. J Comput Phys 2009;228(15):5410–36.

[18] Gottlieb JJ, Groth CPT. Assessment of Riemann solvers for unsteady one-dimensional inviscid flows of perfect gases. J Comput Phys 1988;78:437–58.

[19] Bassi F, Rebay S. A high-order accurate discontinuous finite element method for the numerical solution of the compressible Navier-Stokes equations. J. Comput. Phys. 1997;131:267–79.

[20] Arnold DN, Brezzi F, Cockburn B, Donatella Marini L. Unified analysis of discontinuous Galerkin methods for elliptic problems. SIAM J Numer Anal 2002;39(5):1749–79.

[21] Tadmor E. The numerical viscosity of entropy stable schemes for systems of conservation laws. I. Math Comp 1987;49(179):91–103.

[22] Mock MS. Systems of conservation laws of mixed type. J Differential Equations 1980;37:70–88.

[23] Tadmor E. Entropy functions for symmetric systems of conservation laws. J Math Anal Appl 1987;122:355–9.

[24] Abgrall R, Öffner P, Ranocha H. Reinterpretation and extension of entropy correction terms for residual distribution and discontinuous Galerkin schemes: Application to structure preserving discretization. J Comput Phys 2022;453. http://dx.doi.org/10.1016/j.jcp.2022.110955.

[25] Chandrashekar P. Kinetic energy preserving and entropy stable finite volume schemes for compressible euler and Navier-Stokes equations. Commun Comput Phys 2013;14(5):1252–86. http://dx.doi.org/10.4208/cicp.170712.010313a.

[26] Ranocha H, Dalcin L, Parsani M, Ketcheson DI. Optimized Runge-Kutta methods with automatic step size control for compressible computational fluid dynamics. Commun Appl Math Comput 2022;4(4):1191–228. http://dx.doi.org/10.1007/s42967-021-00159-w.

[27] Gaburro E, Öffner P, Ricchiuto M, Torlo D. High order entropy preserving ADER–DG schemes. Appl Math Comput 2023;440:127644.

[28] Zakerzadeh M. stable and convergent discontinuous Galerkin methods for hyperbolic and viscous systems of conservation laws (Ph.D. thesis), RWTH Aachen University; 2017.

[29] May G, Zakerzadeh M. Class of space-time entropy stable DG schemes for systems of convection–diffusion. Theory, Numer Appl Hyperbolic Probl II 2018;677.

[30] May S. Spacetime discontinuous Galerkin methods for solving convection-diffusion systems. ESAIM Math Model Numer Anal 2017;51(5):1755–81.

[31] Winters AR, Kopriva DA, Gassner GJ, Hindenlang F. Construction of modern robust nodal discontinuous Galerkin spectral element methods for the compressible Navier–Stokes equations. Effic High- Order Discret Comput Fluid Dyn 2021;117–96.

[32] Flad D, Beck A, Munz C-D. Simulation of underresolved turbulent flows by adaptive filtering using the high order discontinuous Galerkin spectral element method. J Comput Phys 2016;313:1–12.

[33] Spiteri RJ, Ruuth SJ. A new class of optimal high-order strong-stability-preserving time discretization methods. Source: SIAM J Numer Anal 2002;40(2):469–91.

[34] Yee HC, Sandham ND, Djomehri MJ. Low-dissipative high-order shock-capturing methods using characteristic-based filters. J Comput Phys 1999;150(1):199–238.

[35] Hu C, Shu C-W. Weighted essentially non-oscillatory schemes on triangular meshes. J Comput Phys 1999;150(1):97–127.

[36] Wang L, Mavriplis DJ. Implicit solution of the unsteady Euler equations for high-order accurate discontinuous Galerkin discretizations. J Comput Phys 2007;225(2):1994–2015.

[37] Mohammed AN, Ismail F. Study of an entropy-consistent Navier–Stokes flux. Int J Comput Fluid Dyn 2013;27(1):1–14.

[38] Gottlieb J, Groth CP. Assessment of Riemann solvers for unsteady one-dimensional inviscid flows of perfect gases. J Comput Phys 1988;78(2):437–58.

[39] Schroeder PW, John V, Lederer PL, Lehrenfeld C, Lube G, Schöberl J. On reference solutions and the sensitivity of the 2D Kelvin–Helmholtz instability problem. Comput Math Appl 2019;77(4):1010–28.

[40] Holmes RL, Dimonte G, Fryxell B, Gittings ML, Grove JW, Schneider M, Sharp DH, Velikovich AL, Weaver RP, Zhang Q. Richtmyer–Meshkov instability growth: Experiment, simulation and theory. J Fluid Mech 1999;389:55–79.

[41] Zhou Y, Williams RJ, Ramaprabhu P, Groom M, Thornber B, Hillier A, Mostert W, Rollin B, Balachandar S, Powell PD, et al. Rayleigh–Taylor and Richtmyer–Meshkov instabilities: A journey through scales. Phys D: Nonlinear Phenom 2021;423:132838.

[42] Roy CJ, Nelson C, Smith T, Ober C. Verification of Euler/Navier–Stokes codes using the method of manufactured solutions. Internat J Numer Methods Fluids 2004;44(6):599–620.